

A global plasma model for reactive deposition of compound films by modulated pulsed power magnetron sputtering discharges

B. C. Zheng, Z. L. Wu, B. Wu, Y. G. Li, and M. K. Lei^{a)}

Surface Engineering Laboratory, School of Materials Science and Engineering,
Dalian University of Technology, Dalian 116024, China

(Received 31 August 2016; accepted 14 February 2017; published online 2 March 2017)

A spatially averaged, time-dependent global plasma model has been developed to describe the reactive deposition of a TiAlSiN thin film by modulated pulsed power magnetron sputtering (MPPMS) discharges in Ar/N₂ mixture gas, based on the particle balance and the energy balance in the ionization region, and considering the formation and erosion of the compound at the target surface. The modeling results show that, with increasing the N₂ partial pressure from 0% to 40% at a constant working pressure of 0.3 Pa, the electron temperature during the strongly ionized period increases from 4 to 7 eV and the effective power transfer coefficient, which represents the power fraction that effectively heats the electrons and maintains the discharge, increases from about 4% to 7%; with increasing the working pressure from 0.1 to 0.7 Pa at a constant N₂ partial pressure of 25%, the electron temperature decreases from 10 to 4 eV and the effective power transfer coefficient decreases from 8% to 5%. Using the modeled plasma parameters to evaluate the kinetic energy of arriving ions, the ion-to-neutral flux ratio of deposited species, and the substrate heating, the variations of process parameters that increase these values lead to an enhanced adatom mobility at the target surface and an increased input energy to the substrate, corresponding to the experimental observation of surface roughness reduction, the microstructure transition from the columnar structure to the dense featureless structure, and the enhancement of phase separation. At higher N₂ partial pressure or lower working pressure, the modeling results demonstrate an increase in electron temperature, which shifts the discharge balance of Ti species from Ti⁺ to Ti²⁺ and results in a higher return fraction of Ti species, corresponding to the higher Al/Ti ratio of deposited films at these conditions. The modeling results are well correlated with the experimental observation of the composition variation and the microstructure transition of deposited TiAlSiN compound films, demonstrating the applicability of this approach in understanding the characteristics of reactive MPPMS discharges as well as the composition and microstructure of deposited compound films. The model for reactive MPPMS discharges has no special limitations and is applicable to high power impulse magnetron sputtering discharges as well. *Published by AIP Publishing.*
[\[http://dx.doi.org/10.1063/1.4977471\]](http://dx.doi.org/10.1063/1.4977471)

I. INTRODUCTION

High power impulse magnetron sputtering (HiPIMS), also known as high power pulsed magnetron sputtering (HPPMS), is a new kind of ionized physical vapor deposition (IPVD) technique developed in recent years.^{1,2} By using unipolar pulses with high power density and low duty cycle,^{3,4} while keeping the average power the same as conventional magnetron sputtering techniques,⁵ a high plasma density of 10¹⁸–10¹⁹ m⁻³ can be produced with a high ionization fraction of the sputtered metal atoms up to 90%.^{6,7} The impact energy and direction of the highly ionized sputtering flux could be controlled by applying a biased voltage to the substrate, resulting in a uniform deposition on complex structures.^{8–10} The densified thin films with improved adhesion could be deposited due to the enhanced adatom mobility and the implanted sputtering species at increased impact energy.^{11–13}

Modulated pulsed power magnetron sputtering (MPPMS),¹⁴ emerged as an alternative of the HiPIMS

technique, provides a high density plasma with a high ionization fraction of sputtered species using a long pulse (also called macropulse), which comprises many micropulses.^{15,16} By modulating the pulse on/off time of the micropulses, the shape and magnitude of a macropulse can be arbitrarily tailored, thus providing more flexible control than HiPIMS.¹⁷

The reactive sputtering technique, where an elemental or alloy target is sputtered in the presence of a reactive gas to deposit compound films, is of significant importance for various applications.¹⁸ As one of the widely used techniques for compound film deposition, lots of models have been developed to investigate the reactive sputtering process.^{19–23} In 1987, Berg *et al.*²² developed a reactive sputtering model in order to understand the hysteresis effect and other characteristics in reactive sputtering deposition. The model was simplified and focused on the most essential processes and could explain the influence of different parameters on the reactive sputtering process qualitatively. In 2014, Berg *et al.*²³ improved the basic model by considering the compound molecule sputtering at the target surface in the form of individual atoms and the implantation of ion species of

^{a)}Author to whom correspondence should be addressed. Electronic mail: mklei@dlut.edu.cn

the reactive gas. Jonsson *et al.*^{19,20} dynamically simulated the pulsed reactive sputtering process and found that under the pulse frequency higher than 100 Hz, the target poisoning, the deposition rate, and the composition of deposited films did not periodically change with the power supply. Kubart *et al.*²¹ developed a model to describe the dynamic behavior of reactive sputtering processes, and the influence of the process parameters on the transient behavior could be well described. Bultinck *et al.*²⁴ simulated a reactive sputtering process of TiN deposition using the particle-in-cell/Monte Carlo collision (PIC/MCC) method; the density and flux of each species in the processing chamber were obtained and the results were verified by the experimental diagnosis.

HiPIMS and MPPMS techniques are particularly promising for reactive sputtering,²⁵ due to the enhanced dissociation of reactive molecular gas and suppressed hysteresis effect.^{26,27} Although some models have been developed for HiPIMS^{28–34} and MPPMS discharges,³⁵ further research is needed for modeling the reactive HiPIMS or MPPMS. Recently, Kozak and Vlcek³⁶ provided a parametric model for reactive HiPIMS by considering specific features of HiPIMS discharges, which makes it possible to calculate the compound fractions at the target surface and the deposition rate at fixed partial pressures of reactive gas. Besides, Gudmundsson *et al.*³⁷ have developed an ionization region model for the reactive HiPIMS discharges, which can apply to an Ar/O₂ HiPIMS discharge with a Ti target in both the metal mode and the poisoned mode. However, the phenomenological model has its limit in investigating the discharge physics, and the modeling work on reactive MPPMS discharges is still lacking.

In this study, a spatially averaged, time-dependent global plasma model has been developed to explore the internal discharge physics during reactive MPPMS pulses. The model was used to describe the TiAlSiN thin film deposition by reactive MPPMS discharges in Ar/N₂ mixture gas, based on the particle balance and the energy balance in the ionization region, and considering the formation and erosion of the compound at the target surface. The introduction of reactive gas species was considered as well, which adds to the complexity of MPPMS discharges. The reactive MPPMS model is an extension of the previous MPPMS discharge model,³⁵ and the numerical procedure is the same as the previous one except that the Hall parameter $\omega_{ge}\tau_c$ is fitted time-dependently, which improves the fitting accuracy during the entire macropulse and is explained in the text below. The time-dependent plasma parameters such as number densities of each species, the electron temperature, and the compound-covered fraction of the target can be obtained by fitting the model to duplicate the experimental discharge currents at different working conditions.

Besides the modeling work, two sets of TiAlSiN deposition processes were performed by reactive MPPMS discharges, and the experimental results of the microstructure and the composition of deposited compound films were compared with the model prediction. The composition, cross-section morphology, and microstructure of the TiAlSiN compound films deposited by MPPMS at the corresponding conditions are investigated by electron probe micro-analysis

(EPMA), scanning electron microscopy (SEM), and high resolution transmission electron microscopy (HRTEM). The composition and microstructure transition of deposited TiAlSiN compound films was well consistent with the model prediction.

II. EXPERIMENTAL DETAILS

TiAlSiN nanocomposite thin films were deposited by a Zpulser AXIATM MPPMS power supply at an average power of 2 kW. Two kinds of TiAlSi alloy targets, Ti_{0.475}Al_{0.475}Si_{0.05} and Ti_{0.3}Al_{0.6}Si_{0.1}, were used as the sputtering target, both of 99.9% purity with an area of 440 × 140 mm² and a thickness of 6 mm. The experiments were performed at a base pressure below 2×10^{-4} Pa. The Ar and N₂ with 99.99% purity were used as the working gas, which were supplied to adjust the working pressures ranging from 0.1 to 0.7 Pa or the N₂ partial pressures f_{N_2} from 0% to 40%. Further details concerning experiments can be found elsewhere.^{35,38}

The pulse shapes of discharges can be arbitrarily tailored by manipulating the micropulse on-time τ_{on} and off-time τ_{off} . Fig. 1 shows the experimental discharge currents and voltage during the modulated macropulses of 800 μ s at different f_{N_2} and different working pressures. The pulses include a 300 μ s weak ionization stage and a 500 μ s strong ionization stage constituted by using different micropulse configurations τ_{off}/τ_{on} of 34/6 μ s and 10/12 μ s, respectively. The discharge voltage around 300 μ s shows a transition from low power discharge to high power discharge adjusted by these power supply generated micropulses. The discharge currents at all conditions are around 15 A during the weakly ionized period of the first 300 μ s, followed by a transition to about 60–250 A during the strongly ionized period of the last 500 μ s, thereby achieving stable discharge processes. The discharge current during the strongly ionized period without N₂ addition is about 150 A and increases to 250 A with N₂ addition. According to the empirical formula of secondary electron emission³⁹

$$\gamma_{SE} = 0.016(E_{iz} - 2\phi), \quad (1)$$

where E_{iz} is the ionization energy of the impacting ion and ϕ is the work function of the target material; the singly charged metal ions hardly meet the condition of secondary electron emission and can be neglected.⁴⁰ However, when the target surface is nitrided, a large portion of N⁺ ions with an ionization energy of 14.5 eV generated by the self-sputtering would bombard the surface and increase the γ_{SE} . Therefore, during the strongly ionized period, which is dominated by self-sputtering, the discharge current is increased with N₂ addition and nitrogen compound formed at the target surface.⁴¹ The corresponding discharge voltages at all conditions are similar to each other at around 400 V as shown in Fig. 1(c).³⁸

TiAlSi amorphous thin films and TiAlSiN nanocomposite thin films were deposited on ultrasonically cleaned Si(100) wafers. The Ti_{0.475}Al_{0.475}Si_{0.05} target was used at different nitrogen partial pressures f_{N_2} of 0%–40% and constant working pressure of 0.3 Pa, and the Ti_{0.3}Al_{0.6}Si_{0.1} target was used at different working pressures of 0.1–0.7 Pa and constant nitrogen partial pressure f_{N_2} of 25%, respectively.

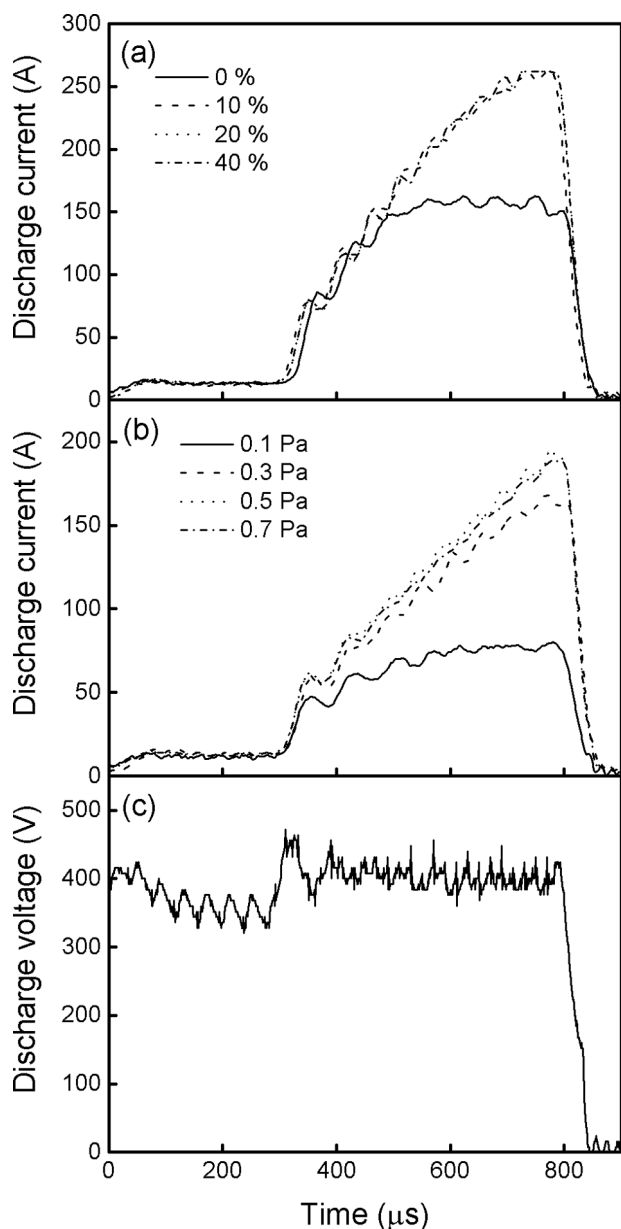


FIG. 1. Experimental discharge currents of reactive MPPMS for depositing TiAlSiN during the modulated macropulses of 800 μs (a) at different nitrogen partial pressures of 0%–40% and constant working pressure of 0.3 Pa and (b) at different working pressures of 0.1–0.7 Pa and constant nitrogen partial pressure of 25%.

The distance between the target and the substrate was kept as 100 mm. In order to remove the surface contaminants, the substrates were cleaned by Ar^+ etching at 2.5 Pa for 20 min by using a pulsed DC bias of -350 V with 100 kHz and 90% duty cycle, and the target surface was sputtered for 2 min before the deposition. The deposition time for all conditions was 60 min.

The chemical composition, the cross-section morphology, and the microstructure of the deposited TiAlSiN thin films were analyzed by using SHIMADZU EPMA-1600 electron probe micro-analysis (EPMA), ZEISS SUPRA 55-32-76 field-emission scanning electron microscopy (FE-SEM) with an operating voltage of 15 kV, and Tecnai G2 20S-TWIN high resolution transmission electron microscopy (HRTEM) with an accelerated voltage of 200 kV. The

samples for HRTEM observation were ground mechanically to foils with a thickness of about 30 μm , which were further thinned down to electron transparency using a Gatan Model 691 precision ion polishing with a 4.5 keV Ar^+ beam at an angle of 3° – 7° . The surface roughness of the deposited TiAlSiN thin films was characterized using a Surfcomer ET4000M surface Profilometer.

III. MODEL DESCRIPTION

A time-dependent global plasma model that was appropriate for elemental target sputtered by noble gas has been developed for the MPPMS discharges,³⁵ based on previous modeling works of steady-state^{42,43} and pulsed plasma discharges.^{30,44–46} Here, the original MPPMS model was extended to describe the TiAlSiN thin film deposition by reactive MPPMS discharges in Ar/N_2 mixture gas and explore its underlying plasma physics. Two additional issues should be addressed for this purpose, one is the nitride compound formed on the target and another is the introduction of N_2 , which adds to the complexity of MPPMS discharges, and both will be discussed below.

A. Formation and erosion balance of the compound at the target

During the reactive MPPMS discharges, the reactive gas species introduced in the chamber may stick to the target surface and form a compound layer. Guttler *et al.*⁴⁷ studied nitrogen distribution at the target surface for a TiN deposition by dcMS discharges in a Ar/N_2 mixture atmosphere and found that the nitrogen distribution along the target surface varied significantly. At the racetrack, the areal density of nitrogen decreases and the balance of the compound formation and erosion shifts towards the erosion. For the HiPIMS and MPPMS discharges, the discharge current at the target surface is significantly higher than the conventional magnetron sputtering, so the compound formation and erosion at the target surface must be considered. Together with the particle balance of each species and the energy balance of the discharge system, the time-dependent plasma parameters such as the number density of each species, the electron temperature, and the compound-covered fraction of the target can be obtained.

Fig. 2 illustrates the schematic diagram of an alloy target containing three components during reactive sputtering, in order to model the TiAlSi alloy targets used in the experiment. The bulk material was divided into three parts M1, M2, and M3 for convenience of mathematical modeling;⁴⁸ therefore, the composition was $[\text{M}1]x_1[\text{M}2]x_2[\text{M}3]x_3$, where $x_1+x_2+x_3=1$. Ignoring the component diffusion during the process, the ratio of sputtered flux of each component should be equivalent to the bulk material. However, the sputtering yield of each component in the alloy target usually differs from each other, resulting in a surface layer with different composition z from the bulk composition x , where $z_1+z_2+z_3=1$. This effect should be considered due to the reaction rate with the reactive species and the flux of each sputtered species from the target surface depends on the components at the target surface rather than the bulk

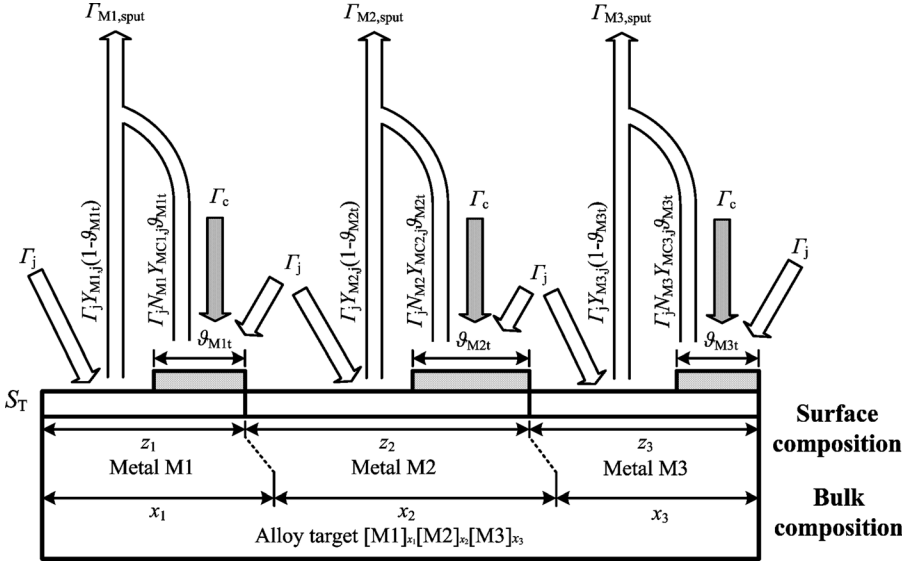


FIG. 2. Schematic diagram of an alloy target containing three components during reactive sputtering.

material. In addition, during the reactive sputtering process, some parts of the surface may react with the reactive gas species and form metal compounds MC1, MC2, and MC3, which occupied the fractions of ϑ_{M1t} , ϑ_{M2t} , and ϑ_{M3t} at the M1, M2, and M3 target surface, and therefore the surface composition was $[M1+MC1]z_1[M2+MC2]z_2[M3+MC3]z_3$. Moreover, in order to take into account the knock-on and direct implantation of reactive gas atoms, and the direct implantation of sputtered metal atoms into the target, a sub-surface compound layer is assumed between the surface layer and the bulk material,^{36,49,50} where the metal compounds MC1, MC2, and MC3 occupy the fractions of ϑ_{M1tb} , ϑ_{M2tb} and ϑ_{M3tb} .

Assume that the compound formation and erosion only occur in the area S_T between the ionization region and the target surface, namely, on the racetrack of the target. The area of $z_i S_T$ was occupied by the i th component, where the fraction of $(1-\vartheta_{Mit})z_i S_T$ was occupied by elemental part Mi and $\vartheta_{Mit}z_i S_T$ by compound part MCi. The sputtered flux of Mi atoms from the target by each ion is

$$\Gamma_{\text{sput,Mi}} = \sum_j \Gamma_j [Y_{Mi,j}(1 - \vartheta_{Mit}) + N_{Mi} Y_{MCi,j} \vartheta_{Mit}], \quad (2)$$

where i is the target component, j is the ion species, Γ_j is the ion flux, N_{Mi} is the number of Mi atoms in the compound molecule MCi, and $Y_{Mi,j}$ and $Y_{MCi,j}$ are the sputtering yields of each species bombarding each elemental metal Mi and compound MCi calculated by the TRIM software,⁵¹ respectively, and the corresponding values are shown in Table I. It can be

TABLE I. Sputtering yields of target metals and compounds at discharge voltage of 400 V, calculated by the TRIM.⁵¹

Y	Ar ⁺	N ₂ ⁺	N ⁺	Al ⁺	Ti ⁺	Si ⁺	Al ²⁺	Ti ²⁺	Si ²⁺
Al	0.57	1.57	1.07	0.90	0.53	0.85	1.31	0.90	1.26
Ti	0.54	0.71	0.51	0.69	0.45	0.66	1.01	0.72	0.96
Si	0.29	0.91	0.64	0.53	0.26	0.49	0.76	0.46	0.74
AlN	0.12	0.39	0.29	0.18	0.11	0.17	0.30	0.22	0.30
TiN	0.35	0.51	0.39	0.43	0.29	0.43	0.63	0.49	0.62
Si ₃ N ₄	0.033	0.11	0.079	0.055	0.030	0.049	0.087	0.057	0.085

seen from Fig. 1(c) that the discharge voltages during the macropulses are around 400 V, so in order to simplify the calculation, the sputtering yields are assumed at ion bombardment energy of 400 eV for singly charged ions, 800 eV for doubly charged ions, and 200 eV for N₂⁺ ions (one molecular ion is dissociated into two atomic ions with half the energy). When the sputtering process achieves its balance, and neglecting the bulk diffusion of each component of the alloy target, the flux ratio of each species sputtered from the target should be the same as the composition ratio of the bulk material

$$z_1 \Gamma_{\text{sput,M1}} : z_2 \Gamma_{\text{sput,M2}} : z_3 \Gamma_{\text{sput,M3}} = x_1 : x_2 : x_3. \quad (3)$$

Therefore, the surface composition could be defined as

$$z_i = \frac{x_i / \Gamma_{\text{sput,Mi}}}{\sum_j x_j / \Gamma_{\text{sput,Mj}}}. \quad (4)$$

Once the surface composition z_i was determined, the three-component alloy target could be seen as three elemental target M1, M2, and M3 with areas of $z_1 S_T$, $z_2 S_T$, and $z_3 S_T$, and the reactive sputtering process could be degraded to the co-sputtering process of three individual sputtering sources.

The adsorption of the reactive gas species at the target surface could happen everywhere, for simplicity, assuming that the adsorption only occurred at non-reacted elemental part at the target surface.⁵² The nitrogen compound formed at the target surface with the introduced reactive gas N₂ was then removed due to the sputtering effect of ion bombardment. The flux of adsorbed reactive gas molecules at the Mi part of $(1-\vartheta_{Mit})z_i S_T$ was $\alpha_{Mit} \Gamma_{c,N_2} (1-\vartheta_{Mit})z_i S_T$, where α_{Mit} is the stick coefficient of the reactive gas species at the target surface i , the values were assumed as 1 for the nitrogen atom and 0.3 for the nitrogen molecule species,⁵³ and Γ_{c,N_2} is the diffusion flux of reactive gas towards the target surface. The sputtered flux of the compound from the target surface is

$$\Gamma_{\text{sput,MCi}} = \sum_j \Gamma_j Y_{MCi,j} \vartheta_{Mit} \quad (5)$$

and the balance equation for the compound-covered fraction of the target can be obtained as^{36,50}

$$\begin{aligned} \frac{d\vartheta_{\text{Mit}}}{dt} \cdot \sigma_{\text{Nt}} = & (N_{\text{N}_2} \alpha_{\text{Mit}, \text{N}_2} \Gamma_{\text{c}, \text{N}_2} + N_{\text{N}} \alpha_{\text{Mit}, \text{N}} \Gamma_{\text{diff}, \text{N}} + N_{\text{N}_2} \alpha_{\text{Mit}, \text{N}_2^*} \Gamma_{\text{diff}, \text{N}_2^*}) (1 - \vartheta_{\text{Mit}}) \\ & + N_{\text{Ci}} \Gamma_{\text{sput}, \text{Mi}} \vartheta_{\text{Mitb}} + (N_{\text{N}_2} \Gamma_{\text{N}_2^+} + N_{\text{N}} \Gamma_{\text{N}^+}) (1 - \vartheta_{\text{Mit}}) \vartheta_{\text{Mitb}} \\ & - N_{\text{Ci}} \Gamma_{\text{sput}, \text{MCI}} - \sum_j \Gamma_j Y'_{\text{MCI}, j} \vartheta_{\text{Mit}} (1 - \vartheta_{\text{Mitb}}) \end{aligned} \quad (6)$$

and

$$\begin{aligned} \frac{d\vartheta_{\text{Mitb}}}{dt} \cdot \sigma_{\text{Ntb}} = & (N_{\text{N}_2} \Gamma_{\text{N}_2^+} + N_{\text{N}} \Gamma_{\text{N}^+}) (1 - \vartheta_{\text{Mitb}}) + \sum_j \Gamma_j Y'_{\text{MCI}, j} \vartheta_{\text{Mit}} (1 - \vartheta_{\text{Mitb}}) \\ & - N_{\text{Ci}} \Gamma_{\text{sput}, \text{Mi}} \vartheta_{\text{Mitb}} - \frac{N_{\text{Ci}}}{N_{\text{Mi}}} \sum_{\text{M}} \Gamma_{\text{M}} \vartheta_{\text{Mitb}}. \end{aligned} \quad (7)$$

The left hand side of Eqs. (6) and (7) is the areal density of the compound molecules, where the reactive atom areal density of the surface monolayer is $\sigma_{\text{Nt}} = n_0^{2/3}$,⁵³ n_0 is the atomic density of the target material, and $\sigma_{\text{Ntb}} = 1.25 \times 10^{20} \text{ m}^{-2}$ is the saturated areal density of compound molecules of the subsurface layer.⁵³ The terms on the right hand side of Eq. (6) are the chemisorption flux of reactive gas species, the exposure of the compound from the bulk layer caused by sputtering of the surface layer, the direct implantation flux of reactive gas ions, the sputtering loss of reactive gas atoms from the target surface layer, and the knock-on implantation flux of reactive gas atoms from the target surface into the subsurface layer, respectively. The first and the last terms on the right hand side of Eq. (7) are the direct implantation fluxes of reactive gas ions and metal ions into the subsurface layer, respectively. N_{Ci} is the number of reactive gas atom in a MCI compound molecule, $N_{\text{N}_2} = 2$ and $N_{\text{N}} = 1$ are the number of reactive gas atom in a reactive gas species, and $\Gamma_{\text{diff}, \text{N}}$, $\Gamma_{\text{diff}, \text{N}_2^*}$, $\Gamma_{\text{N}_2^+}$, and Γ_{N^+} are the flux of each reactive gas species at the target surface. $Y'_{\text{MCI}, j}$ is the knock-on implantation yield calculated by TRIM.⁵¹ By solving the balance equations of compound formation and erosion at the target surface $z_1 S_{\text{T}}$, $z_2 S_{\text{T}}$, and $z_3 S_{\text{T}}$, the variation of compound-covered fractions at the target as well as the surface composition z could be obtained.

Before performing the reactive sputtering process, the magnetron target needs to be cleaned by noble gas sputtering to remove the impurities at the target surface and the compound layer from the previous experiment; therefore, the initial compound-covered fraction of the target is 0. After introducing the reactive gas, the active species generated by the MPPMS discharge during the pulse-on time may react with the target surface, and the formed compound would be removed under the bombardment of the ion current. During the pulse-off time, the plasma was extinct and there are limited active species;⁵⁴ therefore, the compound-cover fraction of the target is assumed to be constant during the pulse-off time. The compound-covered fractions increase with time during each pulse and finally achieve a steady state that ϑ_{Mit} at the beginning of the latter pulse is the same as the former one. The necessary time to achieve this periodic equilibrium state from the model is tens to hundreds of macropulses under typical

MPPMS process parameters, i.e., several seconds, which is consistent with the experimental observation that the discharge current needs several seconds to increase and achieves its steady state. In this state, the modeling result of ϑ_{Mit} is not much changed during one macropulse, and the modeling process is consistent with the real discharge situation.

B. Particle and energy balances of the discharge

The introduction of reactive gas species adds to the complexity of reactive sputtering discharges due to the additional reactions. For simplification, one equivalent excited state of N_2 ($\text{e} + \text{N}_2 \rightarrow \text{N}_2^* + \text{e}$) is considered here,⁴³ while other reactions related to the reactive gas species adopted here can be found in Table II. For the species sputtered from the target, due to the second ionization energy of Ti species from Ti^+ to Ti^{2+} ($E_{\text{iz}, \text{Ti}^+} = 13.58 \text{ eV}$) is even lower than the ionization energy of Ar ($E_{\text{iz}, \text{Ar}} = 15.76 \text{ eV}$), the Ti^{2+} cannot be neglected. In this model, the singly and doubly charged target ion species are considered, and assuming that the target ions are only generated by the single-step energetic electron-impact process, $\text{M} + \text{e} \rightarrow \text{M}^+ + 2\text{e}$, and by Penning ionization, $\text{M} + \text{Ar}^m \rightarrow \text{M}^+ + \text{Ar} + \text{e}$. The electrons, following the previous modeling work,^{33,35} are split up into the hot electron species originated from the secondary emitted electrons, and the cold electrons produced mainly by ionization in the plasma, in order to consider the kinetic effects of secondary electrons in the plasma heating and the ionization processes. The cold electrons are under the assumption of Maxwellian distribution.

Therefore, the primary plasma species include electron e , hot electron e^{H} , working gas species Ar, Ar^+ , Ar^m , and Ar^{H} (hot Ar species which is generated by the recombined Ar^+ on the target, with an equivalent energy of 2 eV ³⁰), reactive gas species N_2 , N_2^+ , N_2^* , N, and N^+ , and target species Al, Al^+ , Al^{2+} , Ti, Ti^+ , Ti^{2+} , Si, Si^+ , and Si^{2+} . The ionization region was assumed as a semi-torus shape hovers above the rectangular racetrack of the target and the detailed geometry can be seen elsewhere.³⁵

By considering the generation and the loss of each species, the rate equations that describe the time-dependent particle densities can be obtained. For nitrogen molecule species, the rate equation is

TABLE II. Principal rate coefficients for Ar/N₂/TiAlSi plasma. The M in Table I refers to the metal species, and the corresponding parameters of a_n , α and β_n are shown in Table III and Table IV.

Reaction	Rate coefficient (m ³ s ⁻¹)	Threshold (eV)	Reference
$e + \text{Ar} \rightarrow \text{Ar}^+ + 2e$	$k_{iz,\text{Ar}} = 2.3 \times 10^{-14} T_e^{0.59} \exp(-17.44/T_e)$	15.76	30
$e^H + \text{Ar} \rightarrow \text{Ar}^+ + 2e$	$k_{iz,\text{Ar}}^H = 8 \times 10^{-14} T_{eH}^{0.16} \exp(-27.53/T_{eH})$	15.76	69,70
$e + \text{Ar} \rightarrow \text{Ar}^m + e$	$k_{ex,\text{Ar}} = 2.5 \times 10^{-15} T_e^{0.74} \exp(-11.56/T_e)$	11.56	30
$e^H + \text{Ar} \rightarrow \text{Ar}^m + e$	$k_{ex,\text{Ar}}^H = 3.85 \times 10^{-14} T_{eH}^{-0.68} \exp(-22.32/T_{eH})$	11.56	69,70
$e + \text{Ar} \rightarrow \text{Ar} + e$ (elastic)	$k_{el,\text{Ar}} = 2.336 \times 10^{-14} T_e^{1.609} \times \exp(0.0618(\ln T_e)^2 - 0.1171(\ln T_e)^3)$		39
$e + \text{Ar}^m \rightarrow \text{Ar} + e$	$k_{dex,\text{Ar}} = 4.3 \times 10^{-16} T_e^{0.74}$	-11.56	30
$e + \text{Ar}^m \rightarrow \text{Ar}^+ + 2e$	$k_{iz,\text{Ar}^m} = 6.8 \times 10^{-15} T_e^{0.67} \exp(-4.2/T_e)$	4.2	30
$e^H + \text{Ar}^m \rightarrow \text{Ar}^+ + 2e$	$k_{iz,\text{Ar}^m}^H = 5.7 \times 10^{-13} T_{eH}^{-0.33} \exp(-6.82/T_{eH})$	4.2	71
$e + \text{N}_2 \rightarrow \text{N}_2^+ + 2e$	$k_{iz,\text{N}_2} = k_{iz,\text{N}_2}^H = 1.95 \times 10^{-15} T_e^{1.13} \times \exp(-14.4/T_e)$	15.6	43
$e + \text{N}_2 \rightarrow \text{N}_2^* + e$	$k_{ex,\text{N}_2} = k_{ex,\text{N}_2}^H = 5.81 \times 10^{-15} \exp(-7.57/T_e)$	6.17	43
$e + \text{N}_2 \rightarrow \text{N}_2 + e$ (elastic)	$k_{el,\text{N}_2} = 1.04 \times 10^{-13} T_e^{0.43} \exp(-0.206/T_e)$		72
$e + \text{N}_2^* \rightarrow \text{N}_2^+ + 2e$	$k_{iz,\text{N}_2^*} = k_{iz,\text{N}_2^*}^H = 3.39 \times 10^{-13} T_e^{-0.176} \times \exp(-32.4/T_e)$		73
$e + \text{N} \rightarrow \text{N}^+ + 2e$	$k_{iz,\text{N}} = k_{iz,\text{N}}^H = 3.84 \times 10^{-15} T_e^{0.92} \times \exp(-12.1/T_e)$	14.54	43
$e + \text{N} \rightarrow \text{N} + e$ (elastic)	$k_{el,\text{N}} = 2.18 \times 10^{-13} T_e^{-0.84} \exp(-0.685/T_e)$		72
$e + \text{N}_2 \rightarrow 2\text{N} + e$	$k_{diss,\text{N}_2} = 6.15 \times 10^{-15} T_e^{0.81} \exp(-12.8/T_e)$	9.76	74
$e + \text{N}_2^+ \rightarrow 2\text{N}$	$k_{diss,\text{N}_2^+} = 1.9 \times 10^{-15} T_e^{-0.30}$		75
$\text{N}_2 + \text{N}^+ \rightarrow \text{N}_2^+ + \text{N}$	$k_{chexc,\text{N}_2-\text{N}^+} = 2.0 \times 10^{-17}$		43
$\text{N} + \text{N}_2^+ \rightarrow \text{N}^+ + \text{N}_2$	$k_{chexc,\text{N}-\text{N}_2^+} = 1.0 \times 10^{-17}$		43
$\text{N}_2^* + \text{N} \rightarrow \text{N}_2 + \text{N}$	$k_{dex,\text{N}_2^*-\text{N}} = 4.0 \times 10^{-17}$	-6.17	43
$\text{N}_2^* + \text{N}_2 \rightarrow 2\text{N}_2$	$k_{dex,\text{N}_2^*-\text{N}_2} = 3.5 \times 10^{-18}$	-6.17	43
$\text{N}_2^* \rightarrow \text{N}_2 + h\nu$	$k_{dex,\text{N}_2^*} = 2.3 \times 10^{-4}$		43
$\text{N}_2 + \text{Ar}^+ \rightarrow \text{N}_2^+ + \text{Ar}$	$k_{chexc,\text{N}_2-\text{Ar}^+} = 1.2 \times 10^{-17}$		43
$\text{Al} + \text{Ar}^m \rightarrow \text{Al}^+ + \text{Ar} + e$	$k_{p,\text{Al}-\text{Ar}^m} = 5.9 \times 10^{-16}$	-5.6	30
$\text{Al} + \text{Ar}^+ \rightarrow \text{Al}^+ + \text{Ar}$	$k_{chexc,\text{Al}-\text{Ar}^+} = 1.0 \times 10^{-15}$		30
$e + \text{Al} \rightarrow \text{Al} + e$ (elastic)	$k_{el,\text{Al}} = 10^{-0.0104(\ln T_e)^2 + 0.1134 \ln T_e - 11.7}$		30
$\text{Ti} + \text{Ar}^m \rightarrow \text{Ti}^+ + \text{Ar} + e$	$k_{p,\text{Ti}-\text{Ar}^m} = 9 \times 10^{-19} \cdot (8kT_{\text{Ar}}/\pi m_{\text{Ti}})^{1/2}$		43
$e + \text{Ti} \rightarrow \text{Ti} + e$ (elastic)	Hard sphere collision		
$e + \text{Si} \rightarrow \text{Si} + e$ (elastic)	Hard sphere collision		
$e + \text{M} \rightarrow \text{M}^+ + 2e$	$k_{iz,\text{M}} = \exp(-E_{iz}/T_e)(T_e/E_{iz})^{1/2} \times \sum_{n=0}^5 a_n [\log_{10}(T_e/E_{iz})]^n$	$E_{iz,\text{M}}$	76
$e + \text{M}^+ \rightarrow \text{M}^{2+} + 2e$	$k_{iz,\text{M}}^H = (T_e/E_{iz})^{-1/2} \times [\alpha \ln(T_e/E_{iz}) + \sum_{n=0}^2 \beta_n (E_{iz}/T_e)^n]$	$E_{iz,\text{M}}$	76

$$\begin{aligned}
\frac{dn_{\text{N}_2}}{dt} = & - \left(k_{iz,\text{N}_2} n_e + k_{iz,\text{N}_2}^H n_{eH} \right) n_{\text{N}_2} - \left(k_{ex,\text{N}_2} n_e + k_{ex,\text{N}_2}^H n_{eH} \right) n_{\text{N}_2} - k_{diss} n_{\text{N}_2} n_e \\
& - \sum_{i=\text{N}^+, \text{Ar}^+} k_{chexc} n_{\text{N}_2} n_i - \sum_{\text{Mi}} \Gamma_{\text{coll}, \text{Mi}} \frac{m_{\text{Mi}}}{m_{\text{N}_2}} \frac{n_{\text{N}_2}}{n_{\text{gas}}} \frac{S_{\text{IR}} - S_{\text{T}}}{V_{\text{IR}}} \\
& - \Gamma_{\text{c}, \text{N}_2} \sum_{\text{Mi}} \alpha_{\text{Mit}, \text{N}_2} (1 - \vartheta_{\text{Mit}}) \frac{z_{\text{Mi}} S_{\text{T}}}{V_{\text{IR}}} + k_{chexc} n_{\text{N}} n_{\text{N}_2^+} \\
& + \sum_{i=\text{N}, \text{N}_2} k_{dex} n_{\text{N}_2^*} n_i + k_{dex, \text{N}_2^*} n_{\text{N}_2^*} + \Gamma_{\text{diff}, \text{N}_2} \frac{S_{\text{IR}} - S_{\text{T}}}{V_{\text{IR}}}, \quad (8)
\end{aligned}$$

where n is the number density, k is the rate coefficient (the fitting expressions are listed in detail in Table II), m is the mass, Γ_{coll} and Γ_{diff} are the flux by “sputtering wind” collision and by diffusional refill, and S_{IR} and V_{IR} are the surface area and the volume of the ionization region, respectively. In Eq. (8), the loss terms are the ionization, excitation, and dissociation collisions with electrons, the charge exchange collisions with N^+ and Ar^+ , the reduction by the “sputtering wind” of the target species, and the reaction with the target surface to form the nitrogen compound; the generation terms are the charge exchange of $\text{N}-\text{N}_2^+$, the de-excitation of N_2^*-N , N_2^*-N_2 , and $\text{N}_2^* \rightarrow \text{N}_2 + h\nu$, and the diffusional refill of

N_2 from the surroundings. It should be mentioned that all of the nitrogen atoms, including the ones created through electron impact dissociation, are assumed at the mean thermal velocity of the gas. However, a significant amount of nitrogen atoms is sputtered out of the target surface and may have much more energy. This effect should be considered in the future work.

For the electrons, the continuity equation is

$$\frac{dn_e}{dt} = \Sigma_e - \Gamma_e \frac{S_{\text{IR}} - S_{\text{T}}}{V_{\text{IR}}}, \quad (9)$$

where Σ_e is the volume-averaged electron source

$$\begin{aligned} \Sigma_e = & (k_{\text{iz,Ar}}n_e + k_{\text{iz,Ar}}^{\text{H}}n_{\text{eH}})(n_{\text{Ar}} + n_{\text{Ar}^{\text{H}}}) + (k_{\text{iz,Ar}^{\text{m}}}n_e + k_{\text{iz,Ar}^{\text{m}}}^{\text{H}}n_{\text{eH}})n_{\text{Ar}^{\text{m}}} + (k_{\text{iz,N}_2}n_e + k_{\text{iz,N}_2}^{\text{H}}n_{\text{eH}})n_{\text{N}_2} + (k_{\text{iz,N}}n_e + k_{\text{iz,N}}^{\text{H}}n_{\text{eH}})n_{\text{N}} \\ & + (k_{\text{iz,N}_2^*}n_e + k_{\text{iz,N}_2^*}^{\text{H}}n_{\text{eH}})n_{\text{N}_2^*} + \sum_i (k_{\text{iz,M}_i}n_e + k_{\text{iz,M}_i}^{\text{H}}n_{\text{eH}})n_{\text{M}_i} + \sum_i (k_{\text{iz,M}_i^+}n_e + k_{\text{iz,M}_i^+}^{\text{H}}n_{\text{eH}})n_{\text{M}_i^+} + \sum_i k_{\text{p,M}_i}n_{\text{M}_i}n_{\text{Ar}^{\text{m}}} \end{aligned} \quad (10)$$

that includes the electrons generated by electron-impact ionization and Penning ionization. The second term on the right hand side of Eq. (9) is the electron loss across the ionization region. The electron flux derived from the drift-diffusion approximation is

$$\Gamma_e = D_e \nabla n_{\text{el}} + \frac{D_e}{T_e} n_{\text{el}} E \approx \frac{D_e}{R} n_{\text{el}} \left(1 + \frac{U_{\text{IR}}}{T_e} \right), \quad (11)$$

where D_e is the Bohm diffusion coefficient and R and U_{IR} are the radius and the potential drop of the ionization region, respectively.³⁵ The electron density on the ionization region boundary can be assumed as $n_{\text{el}} \approx 0.4n_e$ according to the collisionless Langmuir solution for infinite cylinder geometry,³⁹ since the mean free path of momentum exchange λ_{coll} is larger than the characteristic size of the ionization region R at the pressures presented here. Although the ionization region is assumed uniform in this model, a moderate gradient of n_e is expected and assumed on the boundary to include the outward diffusion of electrons. The time-dependent U_{IR} maintains the quasi-neutrality of the plasma and can be obtained by solving the Poisson equation under the assumption of a constant electric field in the ionization region

$$\begin{aligned} U_{\text{IR}} = & -\frac{e \cdot R^2}{\epsilon_0} \left(n_{\text{Ar}^+} + n_{\text{N}_2^+} + n_{\text{N}^+} + \sum_i n_{\text{M}_i^+} \right. \\ & \left. + 2 \sum_i n_{\text{M}_i^{2+}} - n_e - n_{\text{eH}} \right). \end{aligned} \quad (12)$$

The rate equation of e^{H} is³³

$$\frac{dn_{\text{eH}}}{dt} = \frac{1}{eU_{\text{D}}/2} \left(\frac{U_{\text{SH}} \cdot I_{\text{se}}}{V_{\text{IR}}} - Q^{\text{H}} \right), \quad (13)$$

where I_{se} is the secondary electron current

$$I_{\text{se}} = e \sum_j \Gamma_j \sum_i z_i ((1 - \vartheta_{\text{Mit}}) \gamma_{\text{Mi},j} + \vartheta_{\text{Mit}} \gamma_{\text{M}_{\text{Ci}},j}) S_{\text{T}}. \quad (14)$$

In Eq. (14), i is the target component and j is the ion species. The secondary electron emission coefficient γ is obtained by

Eq. (1), where the corresponding ionization energies of the impacting ions can be found in Tables II–IV (the secondary electron emission by the singly charged metal ions is neglected, and only the multiply charged metal ions and the gas ions are considered), and the work function of each target material used here is $\varphi_{\text{Al}} = 4.28 \text{ eV}$,⁵⁵ $\varphi_{\text{Ti}} = 4.3 \text{ eV}$,⁵⁵ $\varphi_{\text{AlN}} = 3.7 \text{ eV}$,⁵⁶ $\varphi_{\text{TiN}} = 3.74 \text{ eV}$,⁵⁷ and $\varphi_{\text{Si}} = 4.85 \text{ eV}$ (the work function of Si_3N_4 is set to the same value as φ_{Si}).⁵⁸ Since some secondary electrons are reabsorbed at the cathode under the influence of the tangential magnetic field, the effective secondary electron emission coefficients are estimated as $\gamma/2$.³⁹ Q^{H} is the energy loss of hot electrons due to inelastic collisions with gas and metal species

$$\frac{Q^{\text{H}}}{e} = \sum_j (E_{\text{j,c}} + E_{\text{htc}}) k_{\text{iz,j}}^{\text{H}} n_{\text{eH}} n_j - E_{\text{dex}} k_{\text{dex}}^{\text{H}} n_{\text{eH}} n_{\text{Ar}^{\text{m}}}, \quad (15)$$

where j is the gas and metal species, $E_{\text{htc}} = 10 \text{ eV}$ is the hot-to-cold population energy transfer when a new electron being created by the hot electron ionization collision falls into the energy range of the cold population,³³ and $E_{\text{j,c}}$ are the inelastic collisional energy losses per electron-ion pair created of each species, where

$$\begin{aligned} k_{\text{iz,Ar}} E_{\text{Ar,c}} &= k_{\text{iz,Ar}} E_{\text{iz,Ar}} + k_{\text{ex,Ar}} E_{\text{ex,Ar}} + k_{\text{el,Ar}} \frac{3m_e}{m_{\text{Ar}}} T_e \\ k_{\text{iz,Ar}^{\text{m}}} E_{\text{Ar}^{\text{m}},c} &= k_{\text{iz,Ar}^{\text{m}}} E_{\text{iz,Ar}^{\text{m}}} + k_{\text{el,Ar}^{\text{m}}} \frac{3m_e}{m_{\text{Ar}}} T_e \\ k_{\text{iz,N}_2} E_{\text{N}_2,c} &= k_{\text{iz,N}_2} E_{\text{iz,N}_2} + k_{\text{ex,N}_2} E_{\text{ex,N}_2} + k_{\text{el,N}_2} \frac{3m_e}{m_{\text{N}_2}} T_e \\ k_{\text{iz,N}} E_{\text{N,c}} &= k_{\text{iz,N}} E_{\text{iz,N}} + k_{\text{el,N}} \frac{3m_e}{m_{\text{N}}} T_e \\ k_{\text{iz,M}_i} E_{\text{M}_i,c} &= k_{\text{iz,M}_i} E_{\text{iz,M}_i} + k_{\text{el,M}_i} \frac{3m_e}{m_{\text{M}_i}} T_e \\ k_{\text{iz,M}_i^+} E_{\text{M}_i^+,c} &= k_{\text{iz,M}_i^+} E_{\text{iz,M}_i^+} + k_{\text{el,M}_i^+} \frac{3m_e}{m_{\text{M}_i^+}} T_e. \end{aligned} \quad (16)$$

By assuming that the electrons are in their thermal equilibrium, the time-dependent electron temperature T_e can be

TABLE III. The parameters of a_n for the electron-impact ionization of Al, Ti, and Si (1×10^{-14} m³/s), and the electron temperature range is $T_e \leq 10E_{iz}$.⁷⁶

Reaction	a_0	a_1	a_2	a_3	a_4	a_5	E_{iz} (eV)
$e + \text{Al} \rightarrow \text{Al}^+ + 2e$	30.8	-28.5	10.5	-2.13	-2.5	2.09	5.96
$e + \text{Al}^+ \rightarrow \text{Al}^{2+} + 2e$	3.46	-3.67	0.44	1.40	-0.54	-0.16	18.83
$e + \text{Ti} \rightarrow \text{Ti}^+ + 2e$	23.0	-18.2	0.03	0.172	2.96	-0.81	6.83
$e + \text{Ti}^+ \rightarrow \text{Ti}^{2+} + 2e$	11.0	-7.09	-3.71	8.00	0.359	-5.36	13.58
$e + \text{Si} \rightarrow \text{Si}^+ + 2e$	25.7	-21.9	5.27	-0.03	-1.25	0.992	8.15
$e + \text{Si}^+ \rightarrow \text{Si}^{2+} + 2e$	6.82	-6.32	2.33	-0.47	-0.55	0.463	16.35

obtained by solving the energy balance equation of the system. The variation of electron energy density with time is

$$\frac{d}{dt} \left(\frac{3}{2} n_e T_e \right) = F_{\text{PWR}} \frac{P_D(t)}{V_{\text{IR}}} - Q - \left(\frac{3}{2} e T_e \Gamma_e \frac{S_{\text{IR}} - S_{\text{T}}}{V_{\text{IR}}} + \sum_i \frac{1}{2} e T_e \Gamma_i \frac{S_{\text{T}} + (S_{\text{IR}} - S_{\text{T}})(1 - \beta_i)}{V_{\text{IR}}} \right). \quad (17)$$

The first term on the right hand side is the external power input, where F_{PWR} is the effective power transfer coefficient and P_D is the discharge power, and the last term is the energy loss of charged particles by leaving the ionization region.³⁵ The energy loss of electrons due to inelastic collisions Q includes the energy losses by electron impact ionization of each species, and the energy gains by de-excitation and Penning ionizations

$$\frac{Q}{e} = \sum_j E_{j,c} k_{iz,j} n_e n_j - E_{\text{dex}} k_{\text{dex}} n_e n_{\text{Ar}^m} - E_{\text{N}_2^+ - \text{N}} k_{\text{N}_2^+ - \text{N}} n_{\text{N}_2^+} n_{\text{N}_2} - E_{\text{N}_2^+ - \text{N}_2} k_{\text{N}_2^+ - \text{N}_2} n_{\text{N}_2^+} n_{\text{N}_2} - \sum_i E_{\text{P}, \text{M}_i} k_{\text{P}, \text{M}_i} n_{\text{M}_i} n_{\text{Ar}^m}. \quad (18)$$

Following the previous work,³⁵ the average ion return fraction β can be estimated as

$$\beta_j = \begin{cases} 0 & U_{\text{IR}} \leq T_j/q_j \\ 1 - \frac{T_j}{q_j U_{\text{IR}}} & U_{\text{IR}} > T_j/q_j, \end{cases} \quad (19)$$

where q_j and T_j are the charge number and the equivalent temperature of j ion species. Adopting the average energy of the sputtered species as $E_{\text{SB}}/2$,⁵⁹ the surface binding energy E_{SB} of each target species can be estimated from the corresponding sublimation enthalpy as 3.38 eV for Al, 4.86 eV for Ti, and 4.67 eV for Si.⁵⁸ The gas temperature is assumed as 0.026 eV.

TABLE IV. The parameters of α and β_n for the hot electron-impact ionization of Al, Ti, and Si (1×10^{-14} m³/s), and the electron temperature range is $T_e > 10E_{iz}$.⁷⁶

Reaction	α	β_0	β_1	β_2	E_{iz} (eV)
$e^{\text{H}} + \text{Al} \rightarrow \text{Al}^+ + 2e$	53.4	-33.9	-8.28	442	5.96
$e^{\text{H}} + \text{Al}^+ \rightarrow \text{Al}^{2+} + 2e$	4.06	-1.47	7.13	-17.9	18.83
$e^{\text{H}} + \text{Ti} \rightarrow \text{Ti}^+ + 2e$	31.1	-7.29	-4.70	70.5	6.83
$e^{\text{H}} + \text{Ti}^+ \rightarrow \text{Ti}^{2+} + 2e$	18.2	-16.9	35.4	36.0	13.58
$e^{\text{H}} + \text{Si} \rightarrow \text{Si}^+ + 2e$	45.2	-28.7	2.66	305	8.15
$e^{\text{H}} + \text{Si}^+ \rightarrow \text{Si}^{2+} + 2e$	11.8	-7.52	-1.83	97.9	16.35

The other rate equations contain no new physics compared with the previous MPPMS discharge model³⁵ and are not given explicitly. The corresponding key reactions for the other primary plasma species during the discharge can be found in Table II.

C. Numerical procedure of the model

The model operates by solving a set of coupled differential equations including the particle balance equations, the energy balance equation, and the balance equations for the compound-covered fractions of the target. Considering the ion and the secondary electron fluxes above the racetrack, the discharge current calculated by the model can be represented as

$$I_{\text{calc}} = e \left(\sum_j \Gamma_j \sum_i z_i (1 - \vartheta_{\text{Mit}}) (q_j + \gamma_{\text{Mi},j}) + \sum_j \Gamma_j \sum_i z_i \vartheta_{\text{Mit}} (q_j + \gamma_{\text{MCI},j}) \right) S_{\text{T}}, \quad (20)$$

where i is the target component, j is the ion species, and q_j is the charge number of j ion species. By fitting the Bohm diffusion coefficient of electrons

$$D_e = \frac{1}{\omega_{ge} \tau_c} \frac{T_e}{B} \quad (21)$$

to reproduce the experimental discharge waveforms, the temporal variation of internal plasma parameters during one modulated macropulse of the reactive MPPMS discharge which corresponds to the real physical situation can be obtained.

The numerical procedure is almost the same as the previous model,³⁵ except that the only one fitting parameter used here is the Hall parameter $\omega_{ge} \tau_c$, which is fitted time-dependently and self-consistently to improve the fitting accuracy during the entire macropulse. This procedure can be realized by using the shooting method to select the appropriate $\omega_{ge} \tau_c$ at each time step to reproduce the experimental discharge currents. Adopting the experimentally measured magnetic field $B = 800$ G at the ionization region boundary, the fitted Hall parameter $\omega_{ge} \tau_c$ varied in the range of 10–20 during the weakly ionized period and 8–10 during the strongly ionized period. Some experimental measurements have been reported by Lundin *et al.*⁶⁰ that a relatively high $\omega_{ge} \tau_c$ of 8–30 is observed in DCMS discharges and a faster-than-Bohm cross-B electron transport (less than 8 or even as low as around 2) may be operating in the HiPIMS discharges. These variations are consistent with the high $\omega_{ge} \tau_c$ values obtained during the weakly ionized period (DCMS-like) of MPPMS discharges and the low $\omega_{ge} \tau_c$ values obtained during the strongly ionized period (HiPIMS-like). However, the underlying mechanism needs to be further studied in the future.

IV. RESULTS

A. Modeling and experimental results at different N_2 partial pressures

The reactive MPPMS discharge processes at different N_2 partial pressures of 0%–40% and constant working pressure of 0.3 Pa are numerically modeled by adopting the experimental

discharge currents of Fig. 1(a) as the input parameters, which was fitted and reproduced by the calculated discharge currents. Fig. 3 shows the modeled electron densities and temperatures during the modulated macropulses of 800 μs at different f_{N_2} . The electron densities n_e at all partial pressures are about $2 \times 10^{18} \text{ m}^{-3}$ at the weakly ionized period and increase sharply during the strongly ionized period, up to $3 \times 10^{19} \text{ m}^{-3}$ at $f_{\text{N}_2} = 10\%$. The maximum of n_e increases from $2.2 \times 10^{19} \text{ m}^{-3}$ to $3 \times 10^{19} \text{ m}^{-3}$ with the addition of the reactive gas N_2 from $f_{\text{N}_2} = 0\%$ to $f_{\text{N}_2} = 10\%$, consistent with the increase in discharge current in this range, and decreases to $2.5 \times 10^{19} \text{ m}^{-3}$ with further increasing f_{N_2} to 40%, due to the fact that the collisional energy loss per electron-ion pair created of molecular gas N_2 is much higher than of Ar.⁴¹ However, the electron temperature T_e has a different trend from n_e , which increases continuously with f_{N_2} . With N_2 addition from $f_{\text{N}_2} = 0\%$ to 10%, the discharge power is increased and both n_e and T_e are improved; with further increasing f_{N_2} to 40%, the discharge power is virtually unchanged and the electron temperature T_e is increased, which is natural from the viewpoint of particle balance and energy balance that the N_2 plasma possesses a higher T_e and lower n_e compared with Ar plasma at constant power density.⁶¹

Rather than the secondary electron heating, the direct Ohmic heating $U_{\text{IR}} \langle I_e \rangle$ has been argued to be the dominant

electron heating mechanism of HiPIMS discharges, at least for Al discharges,³³ where $\langle I_e \rangle$ is the volume-averaged electron current inside the ionization region. According to the estimation by Brenning *et al.*,³¹ the discharge current across the ionization region gradually transforms from ion current domination near the sheath to electron current domination near the bulk plasma, and $\langle I_e \rangle$ could be approximated as $I_D/2$. The effective power transfer coefficient F_{PWR} , which represents the fraction of input power effectively transferred to heat the electrons, can be expressed as³³

$$F_{\text{PWR}} = \frac{eV_{\text{IR}}E_{\text{hlc}}\nu_{\text{iz}}^{\text{H}} + U_{\text{IR}} \cdot \langle I_e \rangle}{P_D} = \frac{eV_{\text{IR}}E_{\text{hlc}}\nu_{\text{iz}}^{\text{H}} + U_{\text{IR}} \cdot I_D/2}{U_D I_D}, \quad (22)$$

where e is the elementary charge, $\nu_{\text{iz}}^{\text{H}}$ is the ionization frequency of the hot electrons with each species, and I_D and P_D are the discharge current and the power input, respectively.

Fig. 4 shows the modeled F_{PWR} of reactive MPPMS discharges during the modulated macropulses of 800 μs at different f_{N_2} . It can be observed that F_{PWR} has the same trend as T_e , which increases at higher N_2 partial pressures f_{N_2} from about 0.04 to more than 0.06 with increasing f_{N_2} from 0% to 40%, due to the fact that the increase of T_e at higher f_{N_2} results in an enhancement of Ohm heating in the ionization region.

Fig. 5 shows the modeled compound-covered fractions of the target at different f_{N_2} . ϑ_{M1t} , ϑ_{M2t} , and ϑ_{M3t} are the compound-covered fractions of AlN , TiN , and Si_3N_4 , respectively. As mentioned at the end of Section III A, the fractions varied during one macropulse and are assumed to be constant during the pulse-off time. The fraction values shown in Fig. 5 are at their periodic equilibrium states, which need tens to hundreds of macropulses, i.e., several seconds under typical MPPMS process parameters to achieve, consistent with the experimental observations. Without N_2 addition, there are no nitrogen compound formed at the target surface and the fractions are 0; with N_2 addition, the fractions increase to about 10% to 40% at $f_{\text{N}_2} = 10\%$ and slow down with further increasing the f_{N_2} . The lower fraction of TiN at the target

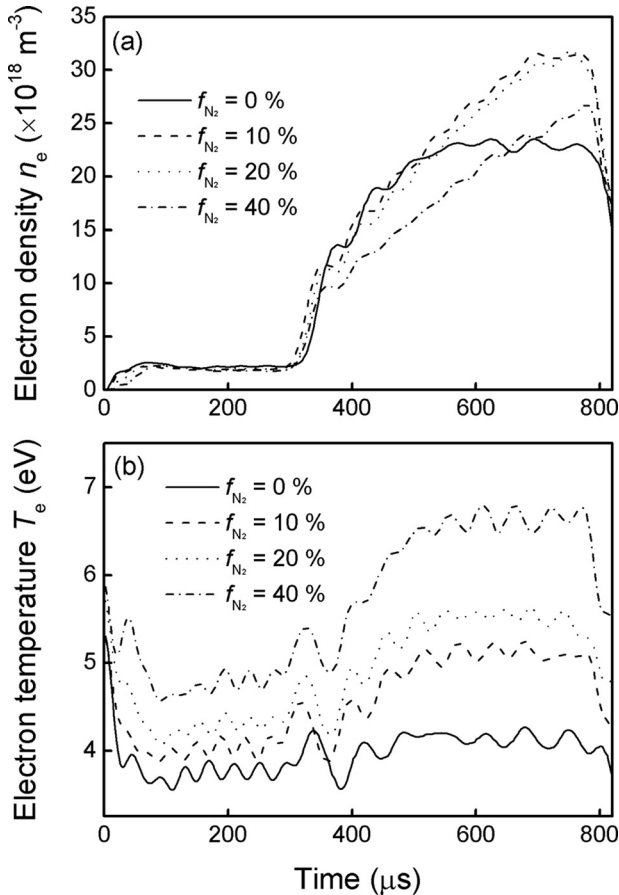


FIG. 3. Modeled electron densities and temperatures of reactive MPPMS discharges for depositing TiAlSiN during the modulated macropulses of 800 μs at a constant working pressure of 0.3 Pa and different f_{N_2} of 0%–40%.

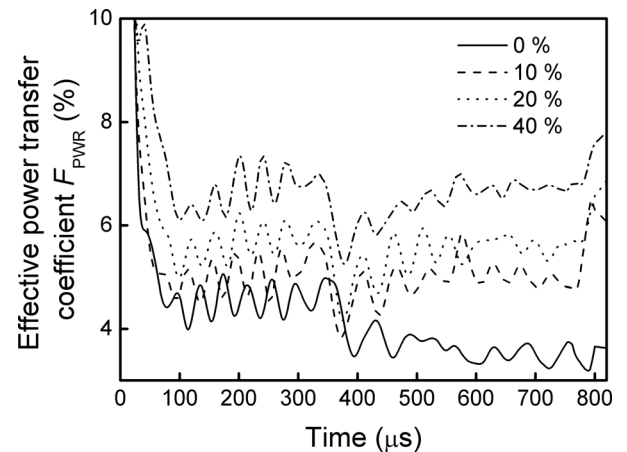


FIG. 4. Modeled effective power transfer coefficients F_{PWR} of reactive MPPMS discharges for depositing TiAlSiN during the modulated macropulses of 800 μs at a constant working pressure of 0.3 Pa and different N_2 partial pressures of 0%–40%.

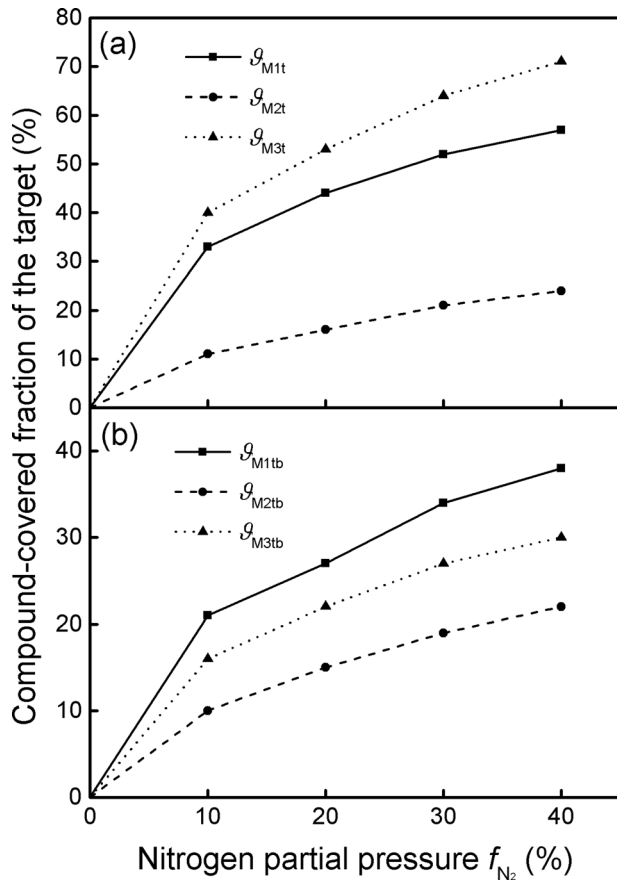


FIG. 5. Modeled compound-covered fractions of the target (a) ϕ_{M1t} and (b) ϕ_{M1tb} of reactive MPPMS discharges for depositing TiAlSiN at a constant working pressure of 0.3 Pa and different N_2 partial pressures of 0%–40%.

surface is due to the much higher sputtering yield of TiN, about 2 to 3 times of AlN and 5 to 10 times of Si_3N_4 computed by TRIM software.⁵¹ The maximal compound-covered fractions of about 40% to 70% at reactive gas partial pressure of 0.12 Pa (at working pressure of 0.3 Pa and f_{N_2} of 40%) were even lower than the 80% at reactive gas partial pressure of 0.01 Pa by conventional dcMS.⁵² This should be due to the fact that gas rarefaction caused by the sputtering wind in HiPIMS discharges reduces the reactive gas flux to the target surface,⁴⁹ together with the limited active particles during pulse-off time, and results in the alleviation of target poisoning.^{54,62} Besides, the specific characteristics of long pulse width and low discharge voltage for the MPPMS process prolongs the target surface erosion at high current densities and reduces the reactive gas ion implantation, respectively, and both contribute to the alleviation of target poisoning.⁶³

In Fig. 5(a), it can be seen that the compound fraction of Si at the target surface ϕ_{M3t} is the highest. It could be understood that since the Si compound has a much lower sputtering yield and sputtering loss than the others, the increase by nitrogen chemisorption dominates the compound balance at the target surface. At the target subsurface, on the contrary, Fig. 5(b) shows that the compound fraction of Si is lower than that of Al ($\phi_{M3b} < \phi_{M1b}$). This may be attributed to the fact that the nitrogen chemisorption plays a significant role in the compound balance; therefore, the lack of nitrogen chemisorption at the subsurface dramatically decreased the

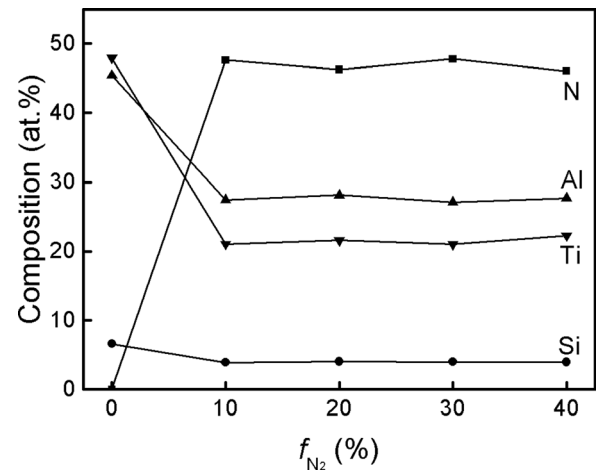


FIG. 6. Composition of TiAlSiN thin films deposited by reactive MPPMS at a constant working pressure of 0.3 Pa and different N_2 partial pressures of 0%–40%.

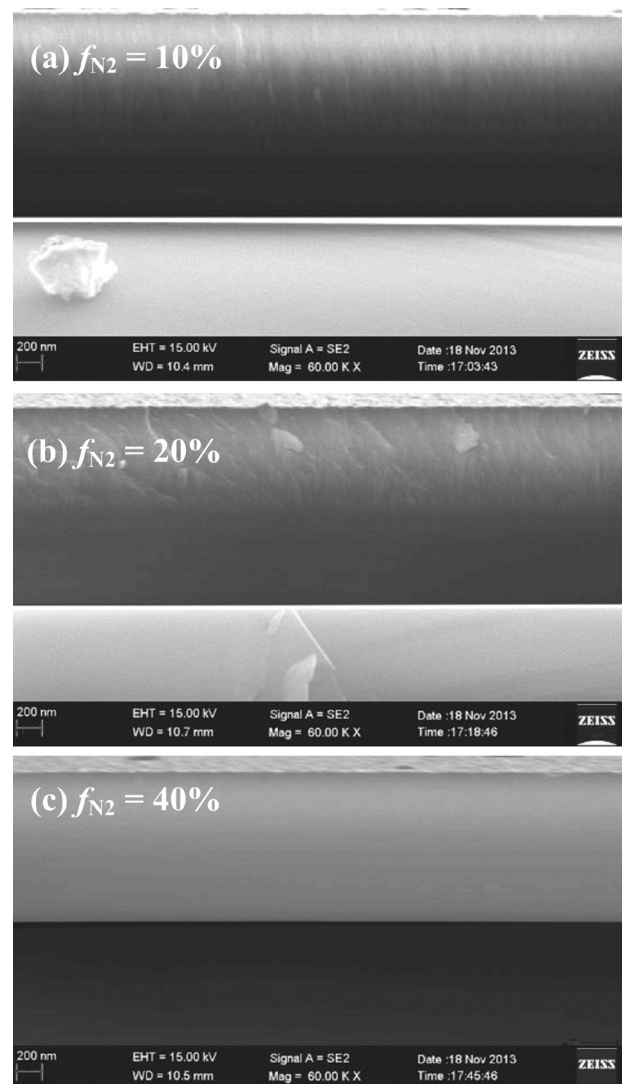


FIG. 7. Cross-section of SEM images of TiAlSiN thin films deposited by reactive MPPMS at a constant working pressure of 0.3 Pa and different N_2 partial pressures of 10%–40%.

source term of the compound and has a greater impact on the Si species, which possesses a much lower sputtering yield.

Fig. 6 shows the composition of TiAlSiN thin films deposited at different f_{N_2} of 0% to 40% measured by EPMA. Without N_2 addition, a TiAlSi alloy thin film was deposited with a composition of $Ti_{0.479}Al_{0.454}Si_{0.066}$, slightly deviated from the target composition of $Ti_{0.475}Al_{0.475}Si_{0.05}$. With N_2 addition of $f_{N_2} = 10\%$, a TiAlSiN thin film with composition of about $Ti_{0.211}Al_{0.274}Si_{0.039}N_{0.476}$ can be achieved and the composition is not much changed with further increasing f_{N_2} . The increase in the Al/Ti composition with increasing the f_{N_2} has been observed recently as well.⁶⁴ The variation of the relative composition of Al and Ti is discussed in more detail in Section V.

Fig. 7 illustrates the cross-section of SEM images of TiAlSiN thin films deposited at different f_{N_2} of 10% to 40%. The deposited thin films are dense under all conditions, and the microstructure gradually transfers from nano-columnar morphology to featureless morphology with increasing the f_{N_2} . The corresponding surface roughness R_a is about 4.7 nm at f_{N_2} of 10% and decreases to about 2.6 nm at f_{N_2} of 40%. The microstructure was identified by HRTEM observations as well, as shown in Fig. 8. At f_{N_2} of 10%, the dark TiAlN nanocrystallines of 5–10 nm were surrounded and separated by the 2–3 nm thick amorphous Si_3N_4 phases, and no voids were observed. The diffraction spots in the corresponding FFT spectrum further confirmed the formation of the nc-TiAlN/a- Si_3N_4 nanocomposite structure. At f_{N_2} of 30%, the grain size of TiAlN nanocrystallines increases to 10–20 nm and the thickness of amorphous Si_3N_4 phases decreases to 1–2 nm, implying an enhancement of phase separation.

B. Modeling and experimental results at different working pressures

Besides modulating the N_2 partial pressure f_{N_2} , another set of experiments were performed at different working pressures of 0.1–0.7 Pa and constant f_{N_2} of 25%. Similarly, by taking the experimental discharge voltages and currents as the input parameters, the MPPMS discharges in the range of 0.1–0.7 Pa are modeled by reproducing the experimental discharge currents, and the plasma parameters during discharges can be obtained.

Fig. 9 shows the modeled electron densities and temperatures of reactive MPPMS discharges for depositing TiAlSiN at different working pressures. The electron density n_e increases from the weakly ionized period (the first 300 μs) to the strongly ionized period (the last 500 μs) at all pressures, which is natural. During the strongly ionized periods, with increasing the working pressure from 0.1 Pa to 0.7 Pa, the n_e increases by up to 5 times while the discharge keeps at similar current densities. This could be explained by the γ_{SE} variation at different pressures: with increasing the working pressure from 0.1 to 0.7 Pa, the covered fraction of nitrogen compounds with lower work function ϕ was increased (data not shown here), and the content of N^+ and N^{2+} ions with higher ionization energy than metal ions was increased as well, which was generated from the self-sputtering of nitrogen compounds at the target surface; both result in an increase of γ_{SE} according to Eq. (1). However, T_e shows an opposite direction to n_e , due to the fact that the increased working pressure and the enhanced sputtering process cool the electrons through collisions. Fig. 10 shows the modeled effective power transfer coefficients F_{PWR} at different

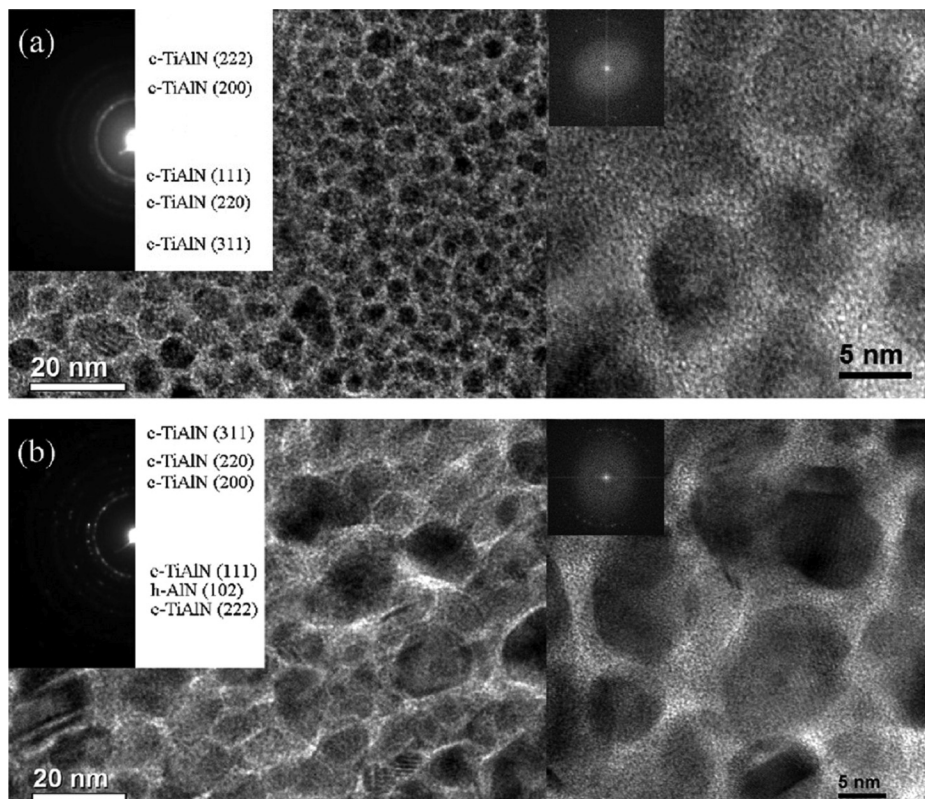


FIG. 8. Cross-section of TEM images of TiAlSiN thin films deposited by reactive MPPMS at a constant working pressure of 0.3 Pa and N_2 partial pressures of 10% and 30%.

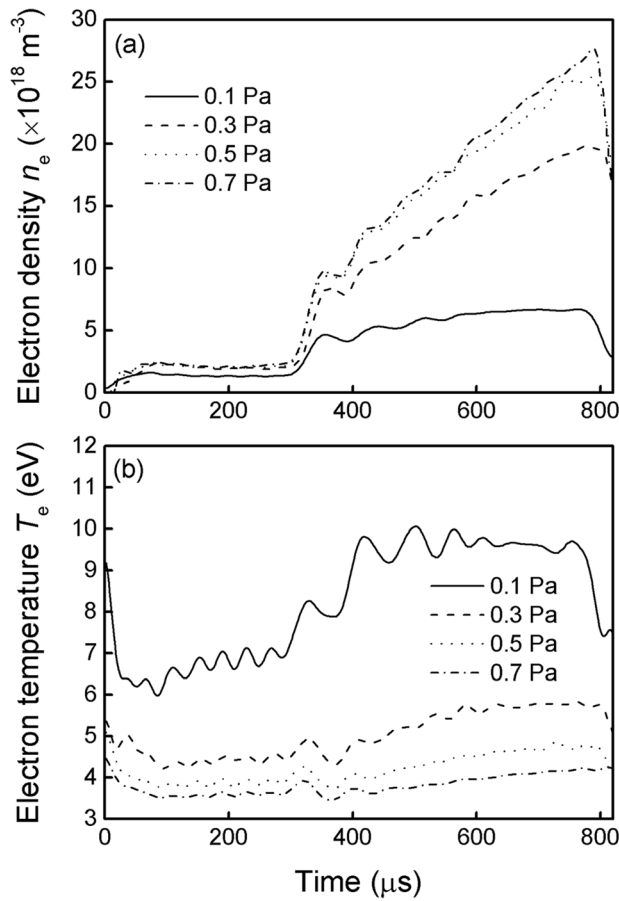


FIG. 9. Modeled electron densities and temperatures of reactive MPPMS discharges for depositing TiAlSiN during the modulated macropulses of 800 μs at constant $f_{N_2} = 25\%$ and different working pressures of 0.1–0.7 Pa.

pressures. Similar to Fig. 4, the oscillations of F_{PWR} match well with T_e and decrease at higher pressures due to the reduction of Ohm heating in the ionization region.

Fig. 11 shows the composition of TiAlSiN thin films deposited at different pressures measured by EPMA. Recalling that the composition of the TiAlSi alloy target used in this set of experiment was $\text{Ti}_{0.3}\text{Al}_{0.6}\text{Si}_{0.1}$, the Al

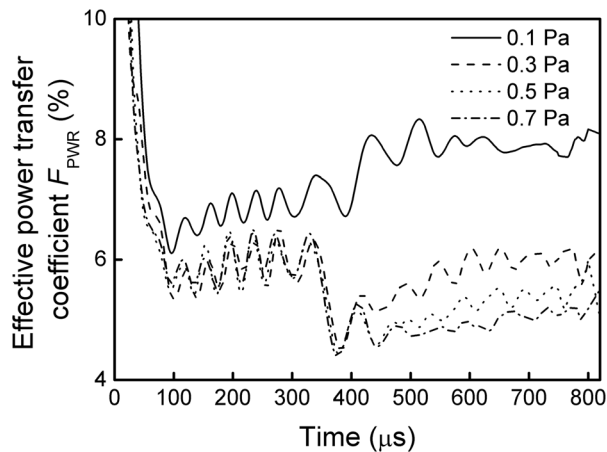


FIG. 10. Modeled effective power transfer coefficients F_{PWR} of reactive MPPMS discharges for depositing TiAlSiN during the modulated macropulses of 800 μs at constant $f_{N_2} = 25\%$ and different working pressures of 0.1–0.7 Pa.

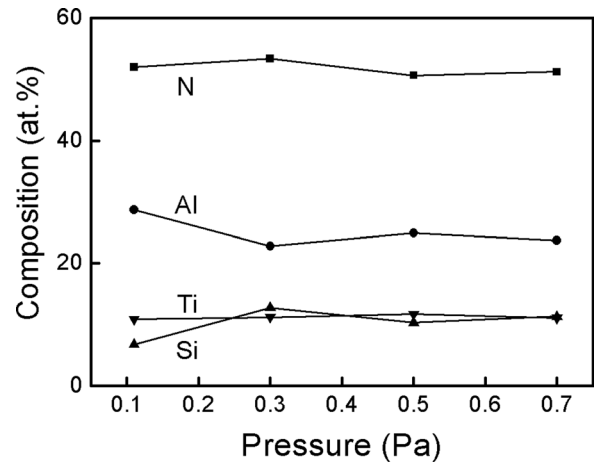


FIG. 11. Composition of TiAlSiN thin films deposited by reactive MPPMS at constant N_2 partial pressure of 25% and different working pressures of 0.1–0.7 Pa.

contents of the compound thin films were about twice as Ti. With increasing the pressure from 0.1 to 0.3 Pa, the Al/Ti content ratio decreases and the composition is not much changed at higher pressures, which is discussed in Section V.

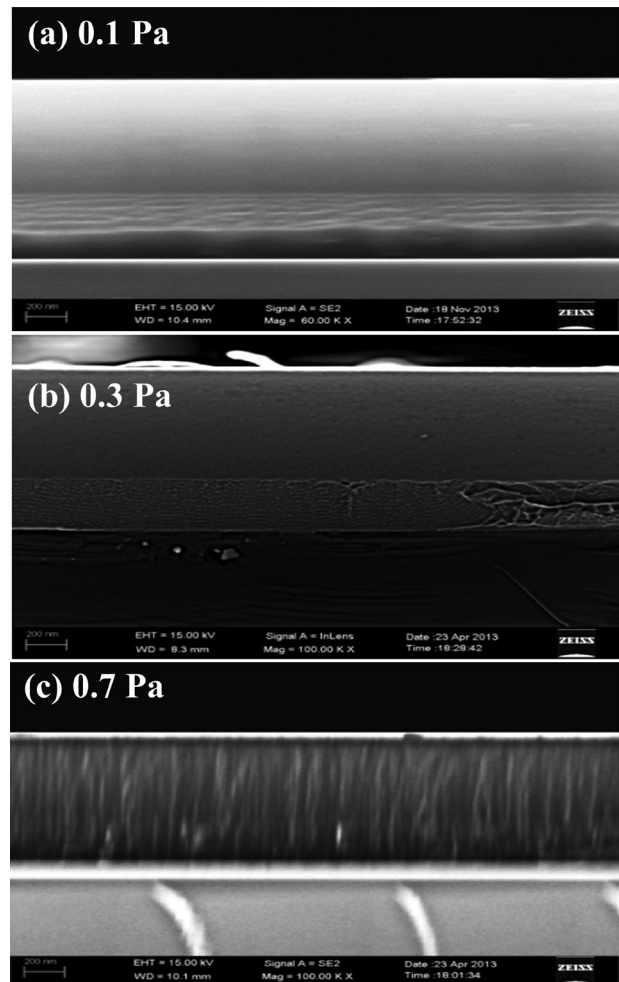


FIG. 12. Cross-section of SEM images of TiAlSiN thin films deposited by reactive MPPMS at a constant N_2 partial pressure of 25% and different working pressures of 0.1–0.7 Pa.

Fig. 12 shows the cross-section of SEM images of TiAlSiN thin films deposited at different pressures. At relatively low pressures of 0.1 and 0.3 Pa, the cross-section of TiAlSiN thin films shows a dense and featureless microstructure, which transfers to columnar grains with increasing the pressure to 0.7 Pa. The corresponding surface roughness increases from 5 nm at 0.1 Pa to 76 nm at 0.7 Pa. Fig. 13 shows the corresponding HRTEM images at pressures of 0.1 and 0.3 Pa. At both pressures, the microstructure of TiAlN nanocrystallines surrounded by amorphous Si_3N_4 phases can be observed. At higher pressures of 0.5 and 0.7 Pa, the structure of nanocrystallines cannot be detected, implying that the phase separation and nanocomposite structure are reduced with increasing the pressure.

V. DISCUSSION

Being superior to the conventional magnetron sputtering, the high ionization fraction of sputtered species in MPPMS or HiPIMS discharges provides a deposition flux mainly consisting of ions of sputtered species instead of atoms; therefore, the variation of discharge conditions and plasma parameters should be considered as the crucial influence on the structure of deposited thin films.⁶⁵ For example, from Fig. 14 it can be seen that the ionization fractions of sputtered species at all conditions presented in this work are about 80% to 90%. Here, similar to our previous work,³⁵ the plasma-dependent deposition parameters directly related to the thin film growth processes, i.e., the kinetic energy of arriving ions and the effective power transferred to the substrate, are adopted rather than the primary process parameters to describe their influence on the composition as well as the microstructure of deposited thin films.

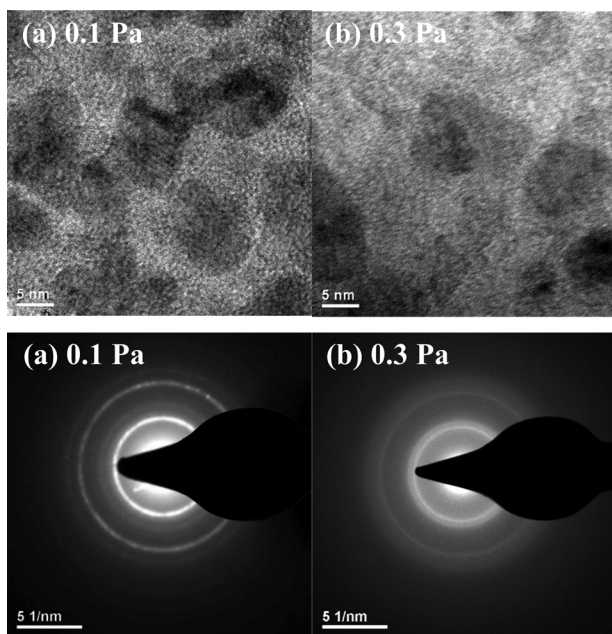


FIG. 13. Cross-section of TEM images of TiAlSiN thin films deposited by reactive MPPMS at a constant N_2 partial pressure of 25% and working pressures of 0.1 Pa and 0.3 Pa.

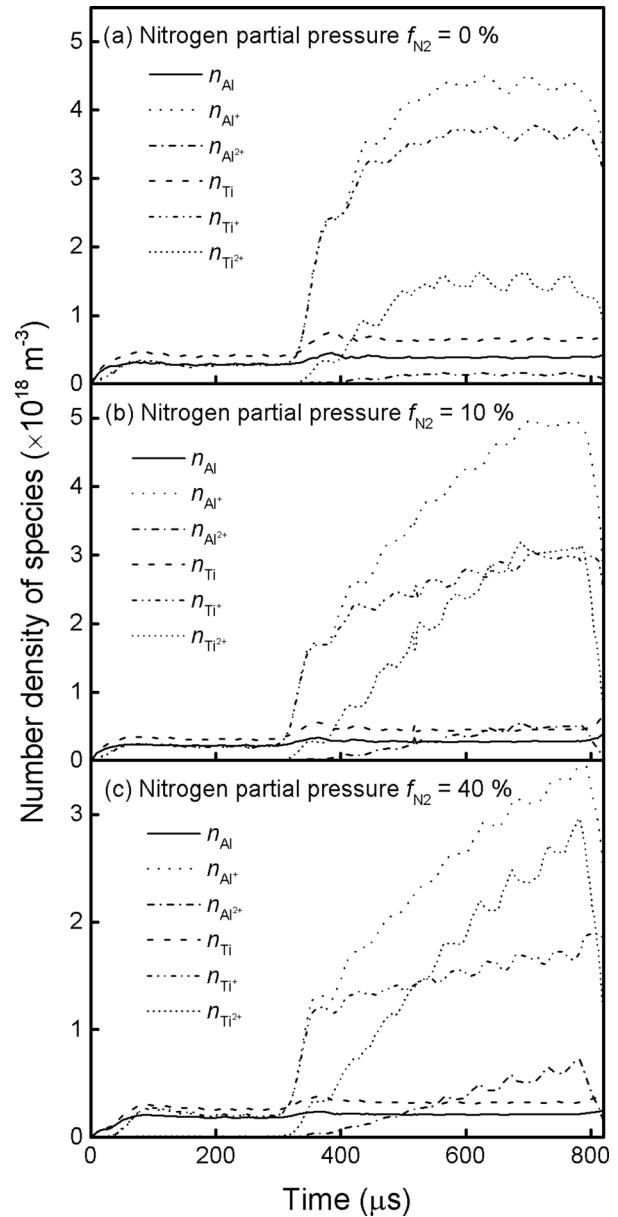


FIG. 14. Modeled number densities of sputtered species of reactive MPPMS discharges for depositing TiAlSiN during the modulated macropulses of 800 μs at a constant working pressure of 0.3 Pa and N_2 partial pressures of 0%, 10%, and 40%.

As mentioned in Eq. (3), by neglecting the bulk diffusion of the alloy target, the flux ratio of each species sputtered from the target should be exactly the same as the composition ratio of the bulk material. However, the difference in ionization fraction and transport behavior of different species leads to a deviation of deposited film composition. As illustrated in Figs. 6 and 11, the Al/Ti content ratio increases with increasing the f_{N_2} from 0% to 10% but decreases with increasing the working pressure from 0.1 to 0.3 Pa, as further increasing the f_{N_2} or the working pressure the Al/Ti content ratio was little changed. To understand the underlying mechanism, Fig. 14 shows the modeled number densities of Al and Ti species during the modulated macropulses of 800 μs at a constant working pressure of 0.3 Pa and N_2 partial pressures of 0%, 10%, and 40%, respectively. The densities of Si species are far

less compared with Al and Ti species and not shown here. Fig. 14(a) shows the number densities of sputtered species without N₂ addition, the dominant sputtered species during the discharge are Al⁺ and Ti⁺ with similar densities, which are about $2.5 \times 10^{17} \text{ m}^{-3}$ during the weakly ionized period and increased to 4.3 and $3.7 \times 10^{18} \text{ m}^{-3}$ during the strongly ionized period, respectively. The doubly charged ions, however, show a larger difference of about $1.1 \times 10^{17} \text{ m}^{-3}$ and $1.5 \times 10^{18} \text{ m}^{-3}$ during the last $300 \mu\text{s}$ for Al²⁺ and Ti²⁺, respectively, due to the lower second ionization energy of Ti (13.58 eV) than Al (18.83 eV). The densities of Al and Ti atoms are rather low during the entire macropulse, which implies the formation of a highly ionized plasma. With N₂ addition, at $f_{\text{N}_2} = 10\%$ shown in Fig. 14(b), the density of Ti²⁺ increases continuously during the pulse-on time and surpasses Ti⁺ at the end of the pulse, up to $3.2 \times 10^{18} \text{ m}^{-3}$. With further increasing the f_{N_2} to 40%, as shown in Fig. 14(c), the density of Ti²⁺ surpasses Ti⁺ at $520 \mu\text{s}$ and continuously increases to $2.9 \times 10^{18} \text{ m}^{-3}$ at the end of the pulse, about 1.5 times of Ti⁺ density. The increase in electron temperature T_e with increasing the N₂ partial pressure f_{N_2} shifts the discharge balance of Ti species from Ti⁺ to Ti²⁺, significantly enhances the production of Ti²⁺ as well as the return fraction of Ti species especially in the f_{N_2} range from 0% to 10%, and results in a higher Al/Ti content ratio of the deposited TiAlSiN thin films in this range. Similarly, at constant nitrogen partial pressure f_{N_2} , the significant decrease of electron temperature in the working pressure ranging from 0.1 to 0.3 Pa reduces the production of Ti²⁺ and the return fraction of Ti species and results in a lower Al/Ti content ratio in this range. Therefore, the variation of charged species at different discharge conditions is believed to be the primary reason for the composition change of compound films.

Similar to the variation of composition, the microstructure and surface roughness of deposited TiAlSiN compound films show an opposite trend with increasing the N₂ partial pressure f_{N_2} or increasing the working pressure. Alami *et al.*⁶⁶ have reported that with increasing the peak target current in HPPMS discharges, the deposited CrN films showed transition from a dense columnar morphology to a nanocrystalline featureless phase. A similar transition has been observed at different f_{N_2} as shown in Figs. 7 and 8, with an increase of discharge current from about 150 A at $f_{\text{N}_2} = 0\%$ to 250 A at $f_{\text{N}_2} = 40\%$. However, with decreasing the working pressure from 0.7 Pa to 0.1 Pa, the same transition occurred while the discharge current was not much changed. As pointed out by Anders,⁶⁵ the microstructure of deposited thin films is mainly influenced by the kinetic energy of deposited ions and the substrate temperature. In this work, all films were deposited without external heating and bias. Therefore, the crucial plasma parameters that influence the microstructure of deposited films are the electron temperature T_e , which determines the floating potential $U_f = -T_e \ln(M/2\pi m)^{1/2}$ (M and m are the mass of the ion and the electron, respectively) and therefore determines the ion bombardment energy, and the effective power transfer coefficient F_{PWR} , which represents the power fraction that effectively heats the electrons and maintains the discharge. In addition, the ion-to-neutral flux ratio incident at the growing

thin film surface is a crucial parameter, which can be estimated by assuming the ion flux out of the ionization region governed by Bohm velocity u_B and the neutral flux by the mean thermal velocity of the gas. The ion fluxes are treated as diffusion to close-lying walls and governed by Bohm velocity, following the previous work of Gudmundsson,⁴⁶ Samuelsson *et al.*,¹² and Raadu *et al.*³⁰ Since the ionization fraction of the sputtered species is not much changed under all conditions (less than 10%, not shown here) and the mean thermal velocity is assumed as the room temperature, the ion-to-neutral flux ratio is approximately proportional to u_B , namely, to $T_e^{1/2}$. By adopting T_e to evaluate the kinetic energy of deposited ions and the ion-to-neutral flux ratio of sputtered species incident at the growing thin film surface, and adopting F_{PWR} to evaluate the substrate heating, the microstructure transition at different f_{N_2} and working pressures can be explained.

With increasing the f_{N_2} from 10% to 40% at a constant working pressure of 0.3 Pa or decreasing the working pressure from 0.7 to 0.1 Pa at constant f_{N_2} of 25%, the ion kinetic energy and ion-to-neutral flux ratio evaluated by T_e and the substrate heating evaluated by F_{PWR} are increased, corresponding to the experimentally observed microstructure transition from the columnar grain structure to the featureless phase, the decrease of surface roughness, and the reduction of phase separation. According to the structure zone diagram (SZD),^{11,56} the microstructure and surface morphology of the deposited thin film are primarily influenced by the diffusion of adatom at the surface. At low f_{N_2} or high working pressure, the surface diffusion is limited since the kinetic energy of arriving ions and the substrate heating are relatively low, and the increased fraction of neutral flux with a wide angular distribution contributes to an increased atomic shadowing, resulting in the columnar grain structure with a high R_a , which can be classified in zone 1 or zone T of the SZD. However, with increasing the f_{N_2} or decreasing the working pressure, the bulk diffusion is negligible but the adatom mobility at the surface is significant, since the kinetic energy of arriving ions, the ion-to-neutral flux ratio, and the substrate heating are increased. Therefore, a transition from a columnar grain structure to a nanocrystalline surrounded by the amorphous phase is observed, due to the fact that the grain growth is periodically interrupted under enhanced ion irradiation.¹¹ The enhanced surface diffusion results in a reduction of surface roughness as well.^{67,68} From Figs. 6 and 11, it can be seen that the film composition in the range of $f_{\text{N}_2} = 10$ to 40% and in the working pressure range of 0.3 to 0.7 Pa is not much changed; therefore, the microstructure transition from the columnar structure to the featureless phase, the phase separation enhancement, and the increase of nanocrystalline grain size should be attributed to the increased input energy to the substrate at higher T_e and F_{PWR} .

Finally, it is worth discussing more about the contribution of charged particles to the discharge current in reactive sputtering discharges. Gudmundsson *et al.*³⁷ demonstrated that the Ar ions contribute a significant portion of the discharge current in the poisoned mode in a Ar/O₂ HiPIMS discharge with a Ti target, and this phenomenon was attributed

to the significantly decreased sputtering yield as low as 0.04 to 0.047 for the Ti species in the poisoned mode. However, since the sputtering yields of the target species have no such dramatic changes between metal and poisoned mode here (data can be seen in Table I), the contribution of Ar ions is around half of the discharge current at all the working pressures from 0.1 to 0.7 Pa and nitrogen partial pressures from 0% to 40% (data not shown here). The contribution of charged particles to the discharge current may vary with the discharge system.

The results presented in this work demonstrate that the composition and microstructure of compound films deposited by MPPMS are influenced by the plasma discharges. A volume-averaged global plasma model is adopted to investigate the influence of process parameters on the plasma parameters as well as on the composition and microstructure of deposited thin films. The modeling results are well correlated with the experimental observation of the variation of the composition, the microstructure, and the surface roughness of deposited TiAlSiN compound thin films at different N₂ partial pressures and working pressures, demonstrating the applicability of this approach in understanding the characteristics of reactive MPPMS discharges, as well as its correlation with the composition and microstructure of deposited compound thin films. The global plasma model for reactive MPPMS discharges presented here has no special limitations and could be applied to HiPIMS discharges as well.

VI. CONCLUSIONS

- (i) A spatially averaged, time-dependent global plasma model has been developed to describe the reactive deposition of the TiAlSiN thin film by modulated pulsed power magnetron sputtering (MPPMS) discharges in Ar/N₂ mixture gas, based on a volume-averaged global description of the ionization region, and considering the formation and erosion of compound at the target surface. The modeling results show an opposite trend of plasma parameters with increasing the N₂ partial pressure from 0% to 40% at a constant working pressure of 0.3 Pa or increasing the working pressure from 0.1 to 0.7 Pa at a constant N₂ partial pressure of 25%. The electron temperature and the effective power transfer coefficient increase with increasing the N₂ partial pressure and decrease with increasing the working pressure.
- (ii) The composition, microstructure, and surface roughness of the deposited TiAlSiN thin films are investigated by EMPA, SEM, TEM, and surface profilometer. A microstructure transition from a columnar grain structure to a featureless nanocrystalline surrounded by amorphous phase with reduced surface roughness has been observed with increasing the N₂ partial pressure or decreasing the working pressure.
- (iii) Using the modeled plasma parameters to evaluate the kinetic energy of arriving ions and the substrate heating, the variations of process parameters that increase both values lead to an enhanced mobility of the adatom at the target surface and an increased input

energy to the substrate, corresponding to the experimental observation of the surface roughness reduction, the microstructure transition from the columnar structure to the dense featureless structure, and the enhancement of phase separation. The increase in electron temperature at higher N₂ partial pressure or at lower working pressure shifts the discharge balance of Ti species from Ti⁺ to Ti²⁺, resulting in a higher return fraction of Ti species as well as a higher Al/Ti ratio of the deposited TiAlSiN thin films. The modeling results contribute to the understanding of the characteristics of reactive MPPMS discharges as well as its correlation with the experimentally observed composition and microstructure transition of deposited compound films.

ACKNOWLEDGMENTS

This work was supported by the National Science Foundation of China under Grant Nos. 51102032, 51575077, and 51621064.

- ¹V. Kouznetsov, K. Macak, J. M. Schneider, U. Helmersson, and I. Petrov, *Surf. Coat. Technol.* **122**, 290 (1999).
- ²J. T. Gudmundsson, N. Brenning, D. Lundin, and U. Helmersson, *J. Vac. Sci. Technol. A* **30**, 030801 (2012).
- ³J. Alami, J. T. Gudmundsson, J. Bohlmark, J. Birch, and U. Helmersson, *Plasma Sources Sci. Technol.* **14**, 525 (2005).
- ⁴J. T. Gudmundsson, P. Sigurjonsson, P. Larsson, D. Lundin, and U. Helmersson, *J. Appl. Phys.* **105**, 123302 (2009).
- ⁵A. Anders, *Surf. Coat. Technol.* **205**, S1 (2011).
- ⁶J. Bohlmark, J. Alami, C. Christou, A. P. Ehasarian, and U. Helmersson, *J. Vac. Sci. Technol. A* **23**, 18 (2005).
- ⁷E. Oks and A. Anders, *J. Appl. Phys.* **105**, 093304 (2009).
- ⁸J. Alami, P. Persson, D. Music, J. T. Gudmundsson, J. Bohlmark, and U. Helmersson, *J. Vac. Sci. Technol. A* **23**, 278 (2005).
- ⁹K. Bobzin, N. Bagcivan, P. Immich, S. Bolz, R. Cremer, and T. Leyendecker, *Thin Solid Films* **517**, 1251 (2008).
- ¹⁰M. Balzer and M. Fenker, *Surf. Coat. Technol.* **250**, 37 (2014).
- ¹¹I. Petrov, P. B. Barna, L. Hultman, and J. E. Greene, *J. Vac. Sci. Technol. A* **21**, S117 (2003).
- ¹²M. Samuelsson, D. Lundin, J. Jensen, M. A. Raadu, J. T. Gudmundsson, and U. Helmersson, *Surf. Coat. Technol.* **205**, 591 (2010).
- ¹³A. P. Ehasarian, J. G. Wen, and I. Petrov, *J. Appl. Phys.* **101**, 054301 (2007).
- ¹⁴R. Chistyakov, B. Abraham, and W. D. Sproul, in *Proceedings of the 49th Annual Technical Conference* (Society of Vacuum Coaters, Washington, D. C., 2006), p. 88.
- ¹⁵J. L. Lin, W. D. Sproul, J. J. Moore, S. Lee, and S. Myers, *Surf. Coat. Technol.* **205**, 3226 (2011).
- ¹⁶F. Papa, H. Gerdes, R. Bandorf, A. P. Ehasarian, I. Kolev, G. Braeuer, R. Tietema, and T. Krug, *Thin Solid Films* **520**, 1559 (2011).
- ¹⁷J. Lin, J. J. Moore, W. D. Sproul, B. Mishra, J. A. Rees, Z. Wu, R. Chistyakov, and B. Abraham, *Surf. Coat. Technol.* **203**, 3676 (2009).
- ¹⁸W. D. Sproul, D. J. Christie, and D. C. Carter, *Thin Solid Films* **491**, 1 (2005).
- ¹⁹L. B. Jonsson, T. Nyberg, and S. Berg, *J. Vac. Sci. Technol. A* **18**, 503 (2000).
- ²⁰L. B. Jonsson, T. Nyberg, I. Katardjiev, and S. Berg, *Thin Solid Films* **365**, 43 (2000).
- ²¹T. Kubart, O. Kappertz, T. Nyberg, and S. Berg, *Thin Solid Films* **515**, 421 (2006).
- ²²S. Berg, H. O. Blom, T. Larsson, and C. Nender, *J. Vac. Sci. Technol. A* **5**, 202 (1987).
- ²³S. Berg, E. Sarhammar, and T. Nyberg, *Thin Solid Films* **565**, 186 (2014).
- ²⁴E. Bultinck, S. Mahieu, D. Depla, and A. Bogaerts, *New J. Phys.* **11**, 023039 (2009).
- ²⁵J. T. Gudmundsson, *Plasma Phys. Controlled Fusion* **58**, 014002 (2016).

- ²⁶M. Hala, R. Vernhes, O. Zabeida, J. E. Klemberg-Sapieha, and L. Martinu, *J. Appl. Phys.* **116**, 213302 (2014).
- ²⁷C. Vitelaru, D. Lundin, N. Brenning, and T. Minea, *Appl. Phys. Lett.* **103**, 104105 (2013).
- ²⁸D. J. Christie, *J. Vac. Sci. Technol. A* **23**, 330 (2005).
- ²⁹J. Vlcek and K. Burcalova, *Plasma Sources Sci. Technol.* **19**, 065010 (2010).
- ³⁰M. A. Raadu, I. Axnas, J. T. Gudmundsson, C. Huo, and N. Brenning, *Plasma Sources Sci. Technol.* **20**, 065007 (2011).
- ³¹N. Brenning, C. Huo, D. Lundin, M. A. Raadu, C. Vitelaru, G. D. Stancu, T. Minea, and U. Helmersson, *Plasma Sources Sci. Technol.* **21**, 025005 (2012).
- ³²C. Q. Huo, M. A. Raadu, D. Lundin, J. T. Gudmundsson, A. Anders, and N. Brenning, *Plasma Sources Sci. Technol.* **21**, 045004 (2012).
- ³³C. Q. Huo, D. Lundin, M. A. Raadu, A. Anders, J. T. Gudmundsson, and N. Brenning, *Plasma Sources Sci. Technol.* **22**, 045005 (2013).
- ³⁴C. Q. Huo, D. Lundin, M. A. Raadu, A. Anders, J. T. Gudmundsson, and N. Brenning, *Plasma Sources Sci. Technol.* **23**, 025017 (2014).
- ³⁵B. C. Zheng, D. Meng, H. L. Che, and M. K. Lei, *J. Appl. Phys.* **117**, 203302 (2015).
- ³⁶T. Kozak and J. Vlcek, *J. Phys. D* **49**, 055202 (2016).
- ³⁷J. T. Gudmundsson, D. Lundin, N. Brenning, M. A. Raadu, C. Huo, and T. Minea, *Plasma Sources Sci. Technol.* **25**, 065004 (2016).
- ³⁸Z. L. Wu, Y. G. Li, B. Wu, and M. K. Lei, *Thin Solid Films* **597**, 197 (2015).
- ³⁹M. A. Lieberman and A. J. Lichtenberg, *Principles of Plasma Discharges and Materials Processing* (John Wiley and Sons Inc., New Jersey, 2005).
- ⁴⁰A. Anders, *Appl. Phys. Lett.* **92**, 201501 (2008).
- ⁴¹F. Magnus, O. B. Sveinsson, S. Olafsson, and J. T. Gudmundsson, *J. Appl. Phys.* **110**, 083306 (2011).
- ⁴²A. J. Lichtenberg and M. A. Lieberman, *J. Appl. Phys.* **87**, 7191 (2000).
- ⁴³K. Tao, D. Mao, and J. Hopwood, *J. Appl. Phys.* **91**, 4040 (2002).
- ⁴⁴S. Ashida, C. Lee, and M. A. Lieberman, *J. Vac. Sci. Technol. A* **13**, 2498 (1995).
- ⁴⁵J. A. Hopwood, *Ionized Physical Vapor Deposition* (Academic Press, San Diego, 2000), Vol. 27.
- ⁴⁶J. T. Gudmundsson, *J. Phys. Conf. Ser.* **100**, 082013 (2008).
- ⁴⁷D. Guttler, R. Grotzschel, and W. Moller, *Appl. Phys. Lett.* **90**, 263502 (2007).
- ⁴⁸M. Moradi, *J. Vac. Sci. Technol. A* **9**, 619 (1991).
- ⁴⁹T. Kubart, M. Aiempnanakit, J. Andersson, T. Nyberg, S. Berg, and U. Helmersson, *Surf. Coat. Technol.* **205**, S303 (2011).
- ⁵⁰K. Strijckmans and D. Depla, *J. Phys. D* **47**, 235302 (2014).
- ⁵¹J. F. Ziegler, M. D. Ziegler, and J. P. Biersack, *Nucl. Instrum. Methods B* **268**, 1818 (2010).
- ⁵²S. Berg and T. Nyberg, *Thin Solid Films* **476**, 215 (2005).
- ⁵³W. Moeller and D. Guettler, *J. Appl. Phys.* **102**, 094501 (2007).
- ⁵⁴M. Aiempnanakit, T. Kubart, P. Larsson, K. Sarakinos, J. Jensen, and U. Helmersson, *Thin Solid Films* **519**, 7779 (2011).
- ⁵⁵A. Anders, J. Andersson, and A. Ehasarian, *J. Appl. Phys.* **102**, 113303 (2007).
- ⁵⁶V. N. Tondare, C. Balasubramanian, S. V. Shende, D. S. Joag, V. P. Godbole, S. V. Bhoraskar, and M. Bhadbhade, *Appl. Phys. Lett.* **80**, 4813 (2002).
- ⁵⁷B. P. Luther, S. E. Mohny, and T. N. Jackson, *Semicond. Sci. Technol.* **13**, 1322 (1998).
- ⁵⁸J. G. Speight, *Lange's Handbook of Chemistry* (McGraw-Hill, New York, 2005).
- ⁵⁹M. W. Thompson, *Philos. Mag.* **18**, 377 (1968).
- ⁶⁰D. Lundin, S. Al Sahab, N. Brenning, C. Huo, and U. Helmersson, *Plasma Sources Sci. Technol.* **20**, 045003 (2011).
- ⁶¹H. Muta, N. Itagaki, and Y. Kawai, *Vacuum* **66**, 209 (2002).
- ⁶²E. Wallin and U. Helmersson, *Thin Solid Films* **516**, 6398 (2008).
- ⁶³M. Hala, J. Capek, O. Zabeida, J. E. Klemberg-Sapieha, and L. Martinu, *J. Phys. D* **45**, 055204 (2012).
- ⁶⁴W. Y. Wu, A. Su, Y. Liu, C. M. Yeh, W. C. Chen, and C. L. Chang, *Surf. Coat. Technol.* **303**, 48 (2016).
- ⁶⁵A. Anders, *Thin Solid Films* **518**, 4087 (2010).
- ⁶⁶J. Alami, K. Sarakinos, F. Uslu, and M. Wuttig, *J. Phys. D* **42**, 015304 (2009).
- ⁶⁷C. L. Chang, S. G. Shih, P. H. Chen, W. C. Chen, C. T. Ho, and W. Y. Wu, *Surf. Coat. Technol.* **259**, 232 (2014).
- ⁶⁸F. Ferreira, R. Serra, J. C. Oliveira, and A. Cavaleiro, *Surf. Coat. Technol.* **258**, 249 (2014).
- ⁶⁹N. J. Mason and W. R. Newell, *J. Phys. B* **20**, 1357 (1987).
- ⁷⁰V. Puech and L. Torchin, *J. Phys. D* **19**, 2309 (1986).
- ⁷¹H. A. Hyman, *Phys. Rev. A* **20**, 855 (1979).
- ⁷²J. T. Gudmundsson, "Electron excitation rate coefficients for the nitrogen discharge," Technical Report No. RH-09-2005 (Science Institute, University of Iceland, 2005).
- ⁷³R. S. Freund, R. C. Wetzel, and R. J. Shul, *Phys. Rev. A* **41**, 5861 (1990).
- ⁷⁴P. C. Cosby, *J. Chem. Phys.* **98**, 9544 (1993).
- ⁷⁵E. G. Thorsteinsson and J. T. Gudmundsson, *Plasma Sources Sci. Technol.* **18**, 045001 (2009).
- ⁷⁶M. A. Lennon, K. L. Bell, H. B. Gilbody, J. G. Hughes, A. E. Kingston, M. J. Murray, and F. J. Smith, *J. Phys. Chem. Ref. Data* **17**, 1285 (1988).